JOURNAL OF GEOPHYSICAL RESEARCH, VOL. 115, A05210, doi:10.1029/2009JA014621, 2010

Click Here for Full Article

Dynamics of ring current and electric fields in the inner magnetosphere during disturbed periods: CRCM–BATS-R-US coupled model

N. Buzulukova,[1] M.-C. Fok,[1] A. Pulkkinen,[1,2] M. Kuznetsova,[1] T. E. Moore,[1] A. Glocer,[1] P. C. Brandt,[3] G. Tóth,[4] and L. Rastätter[1]

Received 2 July 2009; revised 25 November 2009; accepted 10 December 2009; published 15 May 2010.

[1] We present simulation results from a one-way coupled global MHD model (Block-Adaptive-Tree Solar-Wind Roe-Type Upwind Scheme, BATS-R-US) and kinetic ring current models (Comprehensive Ring Current Model, CRCM, and Fok Ring Current, FokRC). The BATS-R-US provides the CRCM/FokRC with magnetic field information and plasma density/temperature at the polar CRCM/FokRC boundary. The CRCM uses an electric potential from the BATS-R-US ionospheric solver at the polar CRCM boundary in order to calculate the electric field pattern consistent with the CRCM pressure distribution. The FokRC electric field potential is taken from BATS-R-US ionospheric solver everywhere in the modeled region, and the effect of Region II currents is neglected. We show that for an idealized case with southward-northward-southward Bz IMF turning, CRCM–BATS-R-US reproduces well known features of inner magnetosphere electrodynamics: strong/weak convection under the southward/northward Bz; electric field shielding/overshielding/penetration effects; an injection during the substorm development; Subauroral Ion Drift or Polarization Jet (SAID/PJ) signature in the dusk sector. Furthermore, we find for the idealized case that SAID/PJ forms during the substorm growth phase, and that substorm injection has its own structure of field-aligned currents which resembles a substorm current wedge. For an actual event (12 August 2000 storm), we calculate ENA emissions and compare with Imager for Magnetopause-to-Aurora Global Exploration/High Energy Neutral Atom data. The CRCM–BATS-R-US reproduces both the global morphology of ring current and the fine structure of ring current injection. The FokRC-BATS-R-US shows the effect of a realistic description of Region II currents in ring current–MHD coupled models.

Citation: Buzulukova, N., M.-C. Fok, A. Pulkkinen, M. Kuznetsova, T. E. Moore, A. Glocer, P. C. Brandt, G. Tóth, and L. Rastätter (2010), Dynamics of ring current and electric fields in the inner magnetosphere during disturbed periods: CRCM–BATS-R-US coupled model, *J. Geophys. Res.*, *115*, A05210, doi:10.1029/2009JA014621.

1. Introduction

[2] The near-Earth space environment is described by multiscale physics that reflects a variety of processes and conditions that occur in magnetospheric plasma. Plasma densities vary from 10^6 cm^{-3} in the F layer of dayside ionosphere to less then 1 cm^{-3} in the tail. Ionospheric plasma is highly collisional, and the plasma above ~500 km is essentially collisionless. It has been recently realized that for a successful description of such a plasma, a complex solution is needed which allows different physics domains to be described using different physical models [*De Zeeuw et al.*, 2004; *Ridley et al.*, 2004; *Tóth et al.*, 2005; *Fok et al.*, 2006; *Zhang et al.*, 2007; *Moore et al.*, 2008]. In the Earth magnetosphere, these domains can be specified as "global magnetosphere," "inner magnetosphere," and "ionosphere."

[3] The traditional approach to simulating the global magnetosphere is magnetohydrodynamics (MHD) modeling. Over the last decades, global 3-D MHD models have proven to be an efficient description of the magnetosphere's dynamic response to solar wind conditions. Basically, several different codes, BATS-R-US [*Powell et al.*, 1999], LFM [*Lyon et al.*, 2004], OpenGGCM [*Raeder et al.*, 2008], and GUMICS [*Laitinen et al.*, 2007] are widely used by the geophysical community. These codes are intensively used to describe idealized events with constant solar wind (SW) and interplanetary magnetic field (IMF), idealized events with

[1]NASA Goddard Space Flight Center, Greenbelt, Maryland, USA.
[2]Goddard Earth Sciences and Technology Center, University of Maryland Baltimore County, Baltimore, Maryland, USA.
[3]Johns Hopkins University Applied Physics Laboratory, Laurel, Maryland, USA.
[4]Center for Space Environment Modeling, University of Michigan, Ann Arbor, Michigan, USA.

Copyright 2010 by the American Geophysical Union.
0148-0227/10/2009JA014621

IMF Bz turning, and real cases with SW input taken from the ACE or WIND spacecrafts. Among the topics addressed with these models are the dynamics of the global magnetosphere during storms [*Goodrich et al.*, 1998; *Rastätter et al.*, 2005], substorm signatures [*Pulkkinen et al.*, 1998; *Raeder et al.*, 2008], steady convection events versus sawtooth events [*Goodrich et al.*, 2007; *Kuznetsova et al.*, 2007], and dayside reconnection physics [*Borovsky et al.*, 2008; *Laitinen et al.*, 2007]. Usually, a separate ionosphere electrodynamics module is used to calculate 2-D electric field patterns from field-aligned currents which are defined by MHD model and given ionospheric conductivities.

[4] While MHD models seem to do a good job in describing global magnetospheric dynamics, they apparently fail to adequately describe the inner magnetosphere. The reason is that MHD assumes that the E × B drift velocity is dominant. This assumption is not valid in the inner magnetosphere where magnetic fields and their gradients are strong. Under such conditions, plasma cannot be treated as single fluid with some velocity and temperature at a given point. Instead, a number of species are usually considered to represent gradient/curvature drifts. Each population has its own energy and drift velocity which is a sum of the gradient/curvature drift and E × B drift. Plasma in this representation is generally anisotropic and is not in a thermodynamic equilibrium. The corresponding transport equations are usually written in terms of bounce-averaged quantities. This approach is sometimes referred to as "drift physics" approach and has proven to be very useful in describing the plasma population of inner magnetosphere with energies from tens of eV to hundreds keV [e.g., *Wolf et al.*, 2007]. This population carries the majority of the plasma pressure and is often referred to as the "ring current" (RC). Models that are based on the drift physics approach are called "ring current models." RC models can also incorporate losses due to the loss cone, charge exchange, and Coulomb interactions, in addition to interactions between different species due to wave activity which are missed in MHD models. For the detailed description of processes which control RC losses, see a review by *Ebihara and Ejiri* [2003].

[5] A general challenge with RC models is in realistically describing the electromagnetic field in the simulation region. This field can be decomposed into a sum of "external" field, which is created outside of the simulation region, and "internal" field that is created by ring current itself. For the sake of simplicity, the "internal" contribution is sometimes omitted. There exist a number of different codes which solve this problem with different assumptions, equations, and numerical methods [e.g., *Ebihara and Ejiri*, 2003].

[6] The simplest solution to this problem is to calculate motion of plasma packets along drift trajectories under prescribed "external" electric and magnetic fields [see, e.g., *Ejiri*, 1978; *Ebihara and Ejiri*, 2000]. The more sophisticated approach is adopted in the Rice Convection Model (RCM). While an externally prescribed magnetic field is assumed, the RCM calculates "internal" electric fields self-consistently with the total pressure distribution [*Jaggi and Wolf*, 1973; *Harel et al.*, 1981; *Toffoletto et al.*, 2003]. Each species is described by one adiabatic invariant (energy invariant), and the particle distribution function is assumed to be isotropic. Self-consistency of the electric field with the plasma distribution is maintained by feedback from the ionosphere via field-aligned currents. A similar RC model, very close to the RCM for dipole magnetic field, is described by *Buzulukova and Vovchenko* [2008].

[7] The Fok Ring Current (FokRC) model [*Fok et al.*, 1995; *Fok and Moore*, 1997] and the Ring Current–Atmosphere Interaction Model (RAM) [*Jordanova et al.*, 1994, 1997; *Liemohn et al.*, 1999] solve the bounce-averaged Boltzmann equation for a number of species with given "external" electric and magnetic fields. Each species is described by two adiabatic invariants μ, K (FokRC model) or, equivalently, energy and equatorial pitch angle (RAM model). The anisotropic pitch angle dependence of distribution function is calculated from the model. The Comprehensive Ring Current Model (CRCM) [*Fok et al.*, 2001] and the Self-Consistent RAM model [*Ridley and Liemohn*, 2002] calculate the "internal" electric fields self-consistently. The equilibrium RCM, RCM-E [*Lemon et al.*, 2004] is a modification of RCM model with "internal" ring current magnetic field model that is calculated from 3-D force equilibrium assumption and treated as a correction to an external empirical magnetic field model. A modification of the RAM model with an "internal" ring current magnetic field also uses a 3-D force equilibrium assumption to calculate corrections to an external empirical magnetic field model [*Zaharia et al.*, 2006]. The Enhanced CRCM model (ECRCM) [*Ebihara et al.*, 2008] is a modification of CRCM model with an "internal" ring current magnetic field that is calculated from the Biot-Savart law and included as a correction to an external empirical magnetic field model.

[8] All these codes are essentially kinetic models because they consider several hundreds different species to describe distribution function of RC plasma. For example, a standard grid in the CRCM consists of 28 points in invariant K and 35 points in invariant μ, so each spacial point contains 980 different species.

[9] An alternative approach was developed by *Fontaine et al.* [1985] and *Peymirat and Fontaine* [1994]. They describe a "fluid" RC model, solving transport equations not for each species but rather for bulk parameters, such as density and temperature. The ring current is represented by only two species: H^+ and e^-. The transport equations have been derived from MHD by modifying the bulk velocity from a pure E × B drift to one that also includes diamagnetic velocities as a proxy for gradient drift. The magnetic field was externally prescribed and electric field was internally calculated to be self-consistent with the pressure distribution. A similar approach has been proposed by *Liu* [2006] where the fluid equations have been derived from bulk-averaged RCM equations. It is very tempting to describe the entire ring current population by only a limited set of equations (instead hundreds as in the case of a kinetic model). Much effort was put into understanding the relations between RCM formalism (such as a drift physics formalism) and fluid formalism [*Heinemann*, 1999; *Heinemann and Wolf*, 2001]. Recently, *Song et al.* [2008] established the equivalence of three models: (1) the fluid model of *Fontaine et al.* [1985] and *Peymirat and Fontaine* [1994] with an additional heat flux describing the energy transfer due to gradient drift; (2) the fluid model of *Liu* [2006] with an assumption that distribution is Maxwellian; (3) the RCM

equations with an assumption that distribution function is not only isotropic as in the original RCM, but also Maxwellian.

[10] However, *Song et al.* [2008] have concluded that all these fluid models produce different results from an original RCM model with a non-Maxwellian distribution function, at least in some test cases. Therefore the description of the inner magnetosphere by fluid models should be done very cautiously.

[11] A more obvious way to combine the MHD approach with inner magnetosphere models has been described by *De Zeeuw et al.* [2004]. The idea is to divide the computational domain into two regions: "outer" magnetosphere and "inner" magnetosphere. The boundary between these two domains is located near the open/closed magnetic field lines boundary. In the outer magnetosphere, only the MHD model is calculated. In the inner magnetosphere, the MHD model runs together with RC model. That is, the MHD model provides the RC model with an "external" B field, electric field potential near the polar cap, and plasma pressure/temperature at the boundary between the two domains (open/closed boundary). The RC model calculates the particle distribution function and "internal" subauroral electric field in the inner magnetosphere. The pressure is then mapped back to the MHD grid (in the region where RC model is calculated) providing a feedback. This approach was called "two-way coupling" to emphasize that RC and MHD models exchange information between each other. *De Zeeuw et al.* [2004] performed two-way coupling of the RCM and BATS-R-US model for the idealized case of southward-northward solar wind Bz turning. The results agree very well with the classical picture of inner magnetosphere electrodynamics: strong convection under southward Bz, overshielding when Bz changes from southward to northward, with weak convection under northward Bz. However, an interesting case of northward to southward Bz turning with substorm development was not considered. Also *De Zeeuw et al.* [2004] found that the pressure peak in his coupled model is significantly larger than in the pure MHD model.

[12] Similar results for idealized conditions were obtained by *Toffoletto et al.* [2004] where one-way coupling of LFM MHD model and the RCM is performed. "One-way" means that there is no feedback of RCM to LFM model, i.e., no pressure correction from the RC model to the MHD model. Only quasi-stationary states were considered and a substorm development due to northward-southward Bz turning was not considered. The results confirm that significant differences occur in the inner magnetospheric pressure distribution result from using a coupled model.

[13] An extensive data-model comparison for real events was performed for the RCM–BATS-R-US coupled model [*Zhang et al.*, 2007; *Welling*, 2009]. The model output was compared with magnetometer data from POLAR, GEOTAIL and GOES satellites and with plasma density/temperature from LANL satellites. It was shown that the RCM–BATS-R-US is very good in reproducing global magnetic field structure but the modeling of plasma variations in the inner magnetosphere remains a challenge.

[14] As mentioned above, the RCM assumes an isotropic particle distribution. The particle losses in the RCM are calculated as a fixed fraction from the full loss cone. RC models like CRCM, FokRC, RAM calculate the evolution of RC distribution function in a more sophisticated and realistic way. From this point of view, coupling these models with MHD can be an important step in understanding RC variations during active periods.

[15] *Keller et al.* [2005] and *Taktakishvili et al.* [2007a] used a one-way coupled BATS-R-US–FokRC ring current model to study ring current buildup during idealized cases of multiple substorms. It was found by *Keller et al.* [2005] that multiple substorms do not increase RC energy. On the contrary, *Taktakishvili et al.* [2007a] showed that BATS-R-US, with kinetic corrections, can reproduce sawtooth oscillations of RC which in turn significantly changes the RC energy. *Taktakishvili et al.* [2007b] modeled two real cases with a one-way coupled FokRC–BATS-R-US model. It was shown that in the first case of 21–22 January 2005, the modeled results are in a reasonable agreement with the data while in the second case of 10–11 August 2000, the agreement is rather poor. It was concluded that some particular tail dynamic is not reproduced in the MHD model. It should also be noted that in both cases geostationary fluxes, on average, were significantly lower (up to several times) in comparison with modeled results.

[16] An idealized substorm study was performed by *Fok et al.* [2006] with the one-way coupled CRCM-LFM model and test-particle code of *Delcourt et al.* [1993, 1994]. A substorm development was initiated by northward-southward solar wind Bz turning in the LFM model. A number of virtual energetic neutral atom images (ENAs) for oxygen atoms were obtained for that idealized substorm. These images then were compared with Imager for Magnetopause-to-Aurora Global Exploration/High Energy Neutral Atom (IMAGE/HENA) oxygen observations for the real case of 28 October 2001. It was concluded that the CRCM–LFM model can describe ring current O^+ injections, at least for an idealized event.

[17] *Fok et al.* [2003] showed modeled hydrogen ENA images for the 15 July 2000 event obtained with FokRC–BATS-R-US model. It is concluded that this model can reasonably describe global RC morphology and that the next logical step is to embed CRCM into the MHD model.

[18] The main purpose of the current work is to introduce improvements to the FokRC–BATS-R-US model and present CRCM–BATS-R-US one-way coupled model with ionospheric feedback. At this stage we do not introduce feedback from the RC model to MHD as in the work of *De Zeeuw et al.* [2004]. The advantage of our approach is that CRCM can more realistically handle the pitch angle distribution of ring current particles than the RCM. We use this advantage to reconstruct ENA images and compare with those from IMAGE/HENA.

[19] In this paper we present both an idealized event with southward-northward-southward IMF Bz turning, and actual event simulations (12 August 2000) with the CRCM–BATS-R-US one-way coupled model. The choice of idealized event is motivated by the need to verify how the new model reproduces stationary states of inner magnetosphere–ionosphere under long periods of northward and southward Bz. We also study transient states such as overshielding/penetration electric field and substorm injection under varying Bz.

[20] The 12 August 2000 storm is chosen as a real case example because IMAGE/HENA captured clear images of

ring current ENA emissions during that time, including images of so-called postmidnight ring current enhancement [*Brandt et al.*, 2002; *Fok et al.*, 2003]. This surprising asymmetry of ring current during the main phase has been explained by characteristic skewing of electric field due to the presence of "internal" electric field and was successfully reproduced by the stand-alone CRCM [*Ebihara and Fok*, 2004; *Fok et al.*, 2003]. We use the CRCM–BATS-R-US model to reproduce IMAGE/HENA images during 12 August 2000 and compare with those images obtained by the IMAGE/HENA instrument. We show that our new model reproduces both the global morphology of the ring current and the fine structure of ring current injection.

[21] Additionally, we calculate the same two events with FokRC–BATS-R-US one-way coupled model. The difference between these two models is only the electric field potential which includes the Region II current effect for CRCM–BATS-R-US, while for FokRC–BATS-R-US it is neglected. By comparing results from the two models in our study, we examine the effect of realistic ionospheric coupling on RC development.

[22] The paper is organized as follows: The methodology of ring current–MHD coupling is described in section 2. Section 3 describes the results for the idealized case of southward-northward-southward Bz turning. The shielding/overshielding/penetration electric field effects are studied in section 3.1; section 3.2 describes Dst*(SYMH*) and pressure profiles for FokRC–BATS-R-US and CRCM–BATS-R-US; section 3.3 describes dynamics of RC pressure and electric fields for CRCM–BATS-R-US model. The results for the 12 August 2000 storm are considered in section 4. The cross polar cap potential is discussed in section 4.1. Section 4.2 shows data-model comparisons of ENA images for two snapshots during storm main phase: the development of a postmidnight RC enhancement at the middle of the main phase, and formation of a RC injection in the evening sector during the early main phase. Section 5 contains the summary, conclusions and directions for future work. Appendices A, B, and C shortly describe the BATS-R-US model, FokRC model and CRCM model and give the relevant references. Appendix D describes the relation between the energy of the modeled RC and Dst/SYMH indices.

2. Coupling Methodology

[23] The Community Coordinated Modeling Center (CCMC) Runs-on-Request System (RoR System) is used to obtain output from the BATS-R-US global MHD model (v.7.73) and Ridley module of Ionosphere Electrodynamics. The BATS-R-US standard settings for the RoR system were used: grid (~$2 \cdot 10^6$ cells) with maximal resolution 0.25 R_E in the inner magnetosphere, magnetosheath and plasma sheet; the Rusanov scheme [*Rusanov*, 1970] with the minmod slope limiter [*van Leer*, 1979] (other limiter and solver options are available in BATS-R-US).

[24] To combine the BATS-R-US and the RC models, we use a similar approach as described by *De Zeeuw et al.* [2004] and *Toffoletto et al.* [2004]. First, the CCMC Kameleon software was used (http://ccmc.gsfc.nasa.gov/downloads/kameleon.php) to process BATS-R-US cdf files. After that we run the RC model in the inner magnetosphere using output from BATS-R-US at each time step as input for the RC model. We do not provide feedback from the RC model to BATS-R-US, so this is a one-way coupled model.

[25] To define the inner magnetosphere and RC modeled region, a regular MLT-λ grid is established in the northern ionosphere between $13° \le \lambda \le 66.8°$. Then every point of the grid is traced along a magnetic field line from BATS-R-US output. This operation is repeated at each MHD output time. A point belongs to the inner magnetosphere if it is located on a closed magnetic field line and the SM equatorial footprint falls in the region $R \le R_B$ where R is a distance from the center of Earth and R_B is some fixed value usually between 8 and 10 R_E. By definition, the low-latitude ionospheric boundary is fixed in time. The polar ionospheric boundary is defined by an evolution of the open/closed boundary and changes in time.

[26] To obtain a solution for ionospheric electric field potential, we use two different solvers: the BATS-R-US solver (Ridley module of Ionosphere Electrodynamics) and the CRCM solver (Sazykin's RCM module). Another important part of the coupling is the definition of electric field potential and ionospheric conductivities. The BATS-R-US solver also calculates the conductivity pattern as a sum of an EUV component and an electron precipitation component. The electron precipitation component is estimated from an empirical relationship between field-aligned currents and ionospheric conductivities, as described by *Ridley et al.* [2004]. To calculate the EUV component, we assume a solar activity index F10.7 = 150×10^4 Jy for the idealized case, and F10.7 = 192.3×10^4 Jy for the 12 August 2000 real event.

[27] To obtain the conductivities and electric potential values needed to run the RC models, the following procedure is performed. First, BATS-R-US values are interpolated to the FokRC/CRCM grid in the northern ionosphere. Second, at every grid point we find the averaged value for electric field potential between the northern hemisphere and correspondent footprint in the southern hemisphere. This value is used as a potential value at the grid point for the northern hemisphere.

[28] The current version of the BATS-R-US solver calculates each hemisphere separately, and in real event simulations sometimes an artificial potential difference is created between the footprints of a field line connecting both hemispheres. An artificial potential difference is produced when the conductance pattern is different due to the tilt angle. In an ideal case, this potential difference should be eliminated by two-way coupling between ionosphere and magnetosphere, creating interhemispheric currents. In practice, this coupling is restricted by grid resolution and numerical diffusion. We have found that the potential difference is negligible if dipole tilt is close to zero. Additionally, we have estimated a value of the above effect for each grid point when the value of dipole tilt was maximal (1000–1200 UT for 12 August 2000). A relative potential difference may be defined as potential difference between two ionospheric footprints divided by the value of cross polar cap potential in northern hemisphere. We have found that the absolute value of relative potential difference is <0.15 for most of grid points and <0.35 for points at the morning flank where the absolute value of potential is large. Equipotentiality is one of the CRCM/FokRC assumptions so

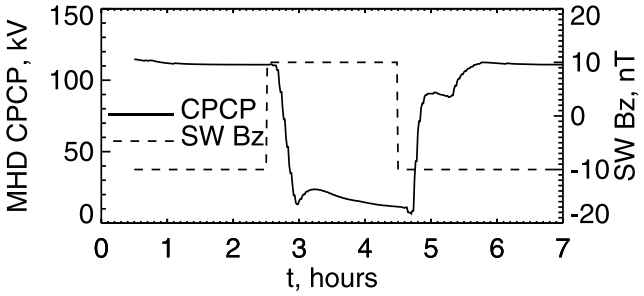

Figure 1. MHD BATS-R-US cross polar cap potential (CPCP) and solar wind Bz for an idealized case.

an averaging procedure is needed to obtain potential for CRCM/FokRC input. The ionospheric conductivity at each grid point is defined as a sum of two values in the northern hemisphere and footprint in the southern hemisphere, so we can take into account the effect from both hemispheres and keep potential constant along field line. The dipole tilt is provided by BATS-R-US and updated together with the magnetic field and other BATS-R-US parameters. The field-line tracing and all field-line integrals are calculated with the BATS-R-US tilt angle.

[29] In the FokRC–BATS-R-US simulations, we define the electric potential at each grid point by this method. In the CRCM–BATS-R-US simulations, we define the electric potential along the polar boundary, then use the CRCM solver to calculate the electric potential equatorward of the polar boundary.

[30] Plasma temperature and density at the polar boundary are calculated from BATS-R-US output at the equatorial footprints of polar boundary points. BATS-R-US temperature and density are converted to H^+/e^- temperatures and density with the following relations [*Toffoletto et al.*, 2004]: $n_{MHD} = n_i = n_e$, $p_{MHD} = n_i kT_i + n_e kT_e$, $T_i/T_e = 7.8$. These parameters are the same for both CRCM and FokRC runs. All MHD data are saved with time interval between 1 and 5 min, and CRCM/FokRC inputs are updated accordingly.

3. Results for Idealized Case of Southward-Northward-Southward Bz Turning

[31] We start with a BATS-R-US run of 7 h duration and a southward-northward-southward Bz orientation. The solar wind and IMF parameters at the BATS-R-US boundary are as follows: $V_x = 400$ km $\cdot s^{-1}$; $V_y = V_z = 0$; n = 5 cm^{-3}; $B_y = B_x = 0$; $P_{dyn} = 1.34$ nPa; -10 nT $< B_z < 10$ nT. The IMF Bz is turned from north to south at t = 2.5 h and from south to north at t = 4.5 h. The duration of the turn is about 1 min. The BATS-R-US output is saved every 1 min. CRCM/FokRC run have been started at t = 0.5 h after MHD results have reached a steady state.

3.1. Electric Field Potential: Shielding, Overshielding, and Penetration Electric Field

[32] The Cross Polar Cap Potential (CPCP) and Bz are shown in Figure 1. There is a characteristic structure of CPCP in response to the variation of Bz: quasi-stationary CPCP ~110 kV at southward Bz corresponds to a strong convection. After the Bz turning at t = 2.5 h, CPCP begins to decrease. There is a delay time ~10–11 min between the Bz turning and the start of CPCP decrease. It takes ~5 min for the new SW conditions to travel from the simulation boundary located at $X_{GSM} = 33\ R_E$ to the bow shock located at $X_{GSM} \sim 15\ R_E$. The additional delay time ~5–6 min is the magnetosphere reaction time, defined by a sum of the travel time of decelerated SW from the bow shock to the magnetopause, and the reaction time of the magnetosphere to the change of conditions on the magnetopause. After the magnetosphere starts to react, the CPCP decreases during the next 15 min.

[33] After the CPCP reaches the minimum at t = 3 h, northward IMF–associated (NBZ) current system [*Iijima and Shibaji*, 1987; *Rasmussen and Schunk*, 1987] begins to develop and causes the CPCP to increase to 20 kV. At t~4.6 h, a southward Bz arrives at the magnetopause and cancels the NBZ current system. A "normal," or typical two-cell convection system begins to return. At t~5 h, the substorm growth phase begins and is followed by reconnection, dipolarization and plasmoid release at t~5.3 h. At the end of the simulation, the profile reaches a plateau of 110 kV, the same as at the beginning of the run. The obtained CPCP profile is very similar to that shown in the works of *Keller et al.* [2005] and *Taktakishvili et al.* [2007b]. Magnetic reconnection which causes a substorm development in this case is controlled by numerical dissipation. We do not introduce here the kinetic corrections to reproduce fast reconnection rates as *Taktakishvili et al.* [2007a, 2008] has done. We are interested in the study of a single isolated substorm and for this purpose numerical dissipation suffices.

[34] Figure 2 shows how the ionospheric electric field responds to both SW/IMF conditions and ring current. We calculate the potential drop ($\Delta\Phi$) along longitude for 5 fixed latitudes (λ = 49.5°, 55.4°, 60.3°, 65.1°, 67.6°) and plot these value as a function of time, t. Figure 2a shows the results for FokRC–BATS-R-US run. For given λ, $\Delta\Phi$ is large for southward Bz. When Bz turned to northward direction it decreases to zero. The potential resulting from the NBZ system is not seen here, because it is confined to high latitudes. The MHD boundary is located at r = 2.5 R_E, so the MHD potential at low latitudes $\lambda < 50.7°$ is equal to

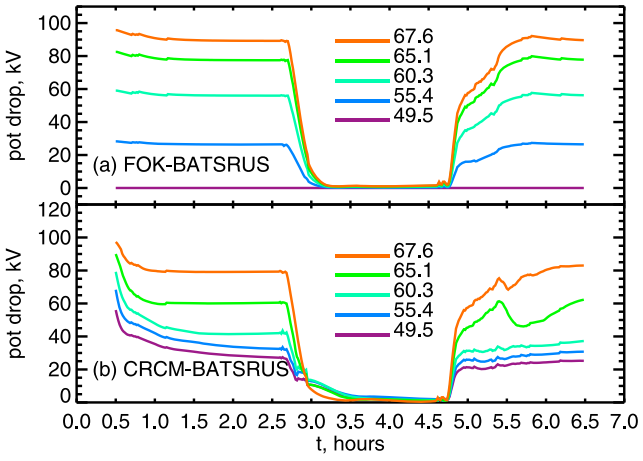

Figure 2. Potential drop in the ionosphere along MLT for a given λ for (a) FokRC–BATS-R-US and (b) CRCM–BATS-R-US models.

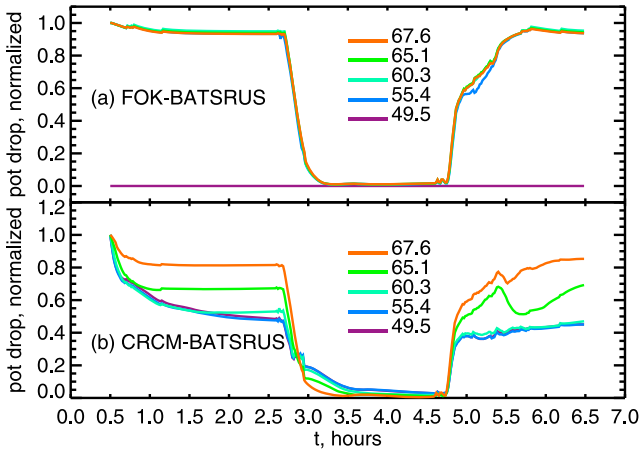

Figure 3. Normalized potential drop in the ionosphere along MLT for a given λ for (a) FokRC–BATS-R-US and (b) CRCM–BATS-R-US models. The potential drop is normalized to a value at the same λ at t = 0.5 h when ring current influence is minimal.

zero. For high values of MHD CPCP, $\Delta\Phi$ is dependent on latitude. The origin of this dependence may be illustrated with uniform dawn-dusk electric field at the equatorial plane. For the dipole B field, $\Delta\Phi = \Phi_0 \cdot L/L_0 = \Phi_0 \cdot \cos^2\lambda_0/\cos^2\lambda$, where Φ_0 is CPCP at the boundary located at λ_0.

[35] The results for the CRCM–BATS-R-US simulation are shown in Figure 2b. The CRCM computational domain is extended to low latitudes (λ = 11.8°), allowing CRCM to describe the potential at low latitudes more realistically. There are shielding effect around t = 2 h and overshielding effect around t = 3 h. However, both overshielding and shielding effects are interfered with the latitude dependence of $\Delta\Phi$. To see directly the effect of the RC, we normalize the obtained value of $\Delta\Phi$ for each time at a given latitude to the value at t_0 = 0.5 h at the same latitude, when the RC influence is minimal. With this normalization, we exclude the latitude dependence from a set of $\Delta\Phi$ at a given time, t.

[36] Figure 3a shows the normalized potential drop $\Delta\Phi_n$ for FokRC–BATS-R-US run. We assume $\Delta\Phi_n = 0$ at λ = 49.5° to emphasize the absence of the electric field. $\Delta\Phi_n$ for other latitudes has the same value at a given time, t, indicating that there is no effect from the ring current. In other words, the electric field penetrates from polar boundary without any decrease, to low latitudes. Furthermore, there are no shielding or overshielding effects. Of course, the condition $\Delta\Phi_n = 0$ at latitudes below 50.7° means "perfect shielding" at those latitudes, but this is an effect of the boundary condition specified in the ionospheric solver and not a ring current effect. Note also that the condition of zero potential means an absence of electric field. From an experimental point of view, this is inaccurate, at least for disturbed periods with strong penetrating electric field [see, e.g., *Huang et al.*, 2007].

[37] The results for the CRCM–BATS-R-US simulation are shown in Figure 3b. At t = 0, all plots start from the same value, as expected. At t = 2 h, $\Delta\Phi_n$ = 0.55 at λ = 49.5°, 55.4°, 60.3°, $\Delta\Phi_n$ = 0.65 at λ = 65.1° and $\Delta\Phi_n$ = 0.8 at λ = 65.1°. In other words, the normalized potential drop has a higher value at higher latitudes. This signals the weakening of the electric field at low latitudes and demonstrates the shielding effect. The shielding, however, is not perfect at low latitudes in the sense that the electric field is not zero. Assuming that the measure of shielding in this case is the ratio $\Delta\Phi_{n,\ \text{CRCM-BATSRUS}}/\Delta\Phi_{n,\ \text{FokRC-BATSRUS}}$, we find that the ring current weakens the potential at low latitudes by a factor two. The shielding lasts during the entire time interval in which the IMF Bz component is directed southward. When the CPCP starts to decrease due to the arrival of northward Bz, the potential drop at all latitudes decreases accordingly. Beginning at t = 2.9 h, the minimum value of $\Delta\Phi_n$ occurs at the highest latitude. This signals on overshielding effect. The maximum effect takes place during the 30 min after Bz turning, but the residual effect lasts during all interval of northward Bz. At t = 4.7 h, southward Bz arrives at the magnetopause, and $\Delta\Phi_n$ starts to increase at all latitudes. There is a short time interval 4.7 h < t < 4.8 h during which $\Delta\Phi_n$ has the same value at all latitudes, signaling the direct penetration of the electric field. For that idealized case, the duration of the effect is about 10 min. After that time interval, the shielding begins to recover. An injection signature is clearly seen around t = 5.5 h when $\Delta\Phi_n$ starts to decrease at λ = 65.1° and at λ = 67.6°. It takes place after a reconnection event occurs at t = 5.3 h (Figure 1). Simultaneously, the dipolarization takes place and an inductive electric field is formed, pushing particles into the inner magnetosphere and producing even stronger shielding. Geostationary orbit falls into the region where the injection signature is seen ($\lambda \sim 67°$).

[38] From Figure 3b we extract shielding/overshielding/penetration characteristic times for the idealized event. When strong convection is imposed on weak ring current at $t = t_0$, the shielding formation time is ~0.5 h at high latitudes (λ = 65.1°, 67.6°), and ~2–2.5 h at low latitudes (λ = 60.3°, 55.4°, 49.5°). The overshielding is more expressed during ~0.5 h after the CPCP decrease. The direct penetration of electric field lasts ~10 min after the sharp CPCP increase. After that, the shielding at low latitudes is reestablished by preexisting RC.

3.2. Ring Current Energy (Dst*) and Pressure Radial Profiles

[39] Figure 4 shows Dst* for the FokRC–BATS-R-US and CRCM–BATS-R-US runs (see Appendix D for Dst* derivation). Dst* starts from the same value in both runs.

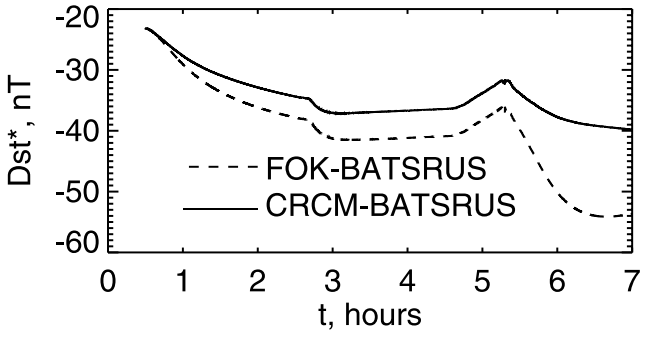

Figure 4. The Dst* index calculated from the ring current energy using the DPS relation for FokRC–BATS-R-US and CRCM–BATS-R-US models.

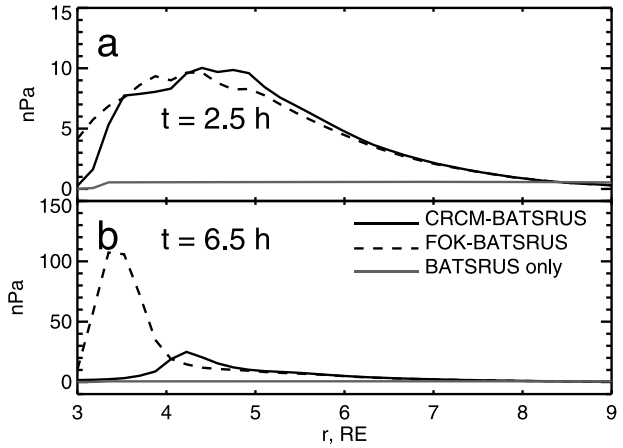

Figure 5. Radial pressure profiles (MLT = 0000 h) for FokRC–BATS-R-US, CRCM–BATS-R-US, and BATS-R-US only runs (a) under stationary strong convection and (b) in the end of the run after the injection occurs. The Y scale is different for Figures 5a and 5b.

Dst* is nonzero because the inner magnetosphere is filled with preexisted RC calculated from empirical model of *Sheldon and Hamilton* [1993]. During the period of southward Bz, Dst* for both runs decreases. At t = 2.7 h, Dst* = −32 nT for the CRCM–BATS-R-US run and Dst* = −37 nT for the FokRC–BATS-R-US run. This difference comes from the shielding effect in the CRCM that prevents particles from entering the inner magnetosphere. At t = 2.7 h, Dst* starts to decrease more rapidly when northward Bz strikes the magnetopause causing a decrease in CPCP and electric field intensity. This is an effect of the inductive electric field. The inductive electric field is included explicitly in CRCM and the induced drift velocity is calculated from the instantaneous velocity of the magnetic field tube motion in response to temporal variation of the magnetic field [*Fok et al.*, 1996]. When northward Bz arrives at the magnetopause, the magnetosphere starts to change configuration from more stretched at the nightside and a more compressed at the dayside to more dipole-like configuration. The inductive electric field (motion of magnetic field lines) moves particles to the Earth at the nightside and away from the Earth at the dayside. This is similar to the effect of the dawn-dusk electric field. The RC at this time is asymmetric (see Figure 6) and concentrated at the nightside, so the inductive electric field causes an energization of the ring current. This effect lasts ~10 min while the magnetosphere adjusts its configuration, so the total change in Dst* is small in this case, about 5 nT for both runs.

[40] During the time interval 3 h < t < 4.6 h, Dst* recovers slowly. At t = 4.7 h, southward Bz arrives at the magnetopause and the magnetosphere starts to stretch at the nightside and compress at the dayside. The RC at this time is almost symmetric (see Figure 6). The induction electric field at the nightside is directed opposite the to convection and prevents the new population from entering the inner magnetosphere. At the dayside, the convection electric field tries to remove particles from the inner magnetosphere while the induction electric field has the opposite effect. Because the induction electric field is stronger at the nightside, the net effect causes Dst* to increase for both runs. Dst* increases until the reconnection and dipolarization injection start to develop at t = 5.4 h. At the end of the injection, at t = 6.5 h, a noticeable increase in Dst* arises (about 15 nT) in both runs. Again the reason is that the shielding of electric field prevents particle from entering the inner magnetosphere. We can now estimate the effect of a single isolated injection on ring current buildup: the Dst* change due to the injection equals ~ −7nT for CRCM–BATS-R-US and ~ −17nT for FokRC–BATS-R-US. The results for the FokRC–BATS-R-US simulation presents the limiting case of zero shielding. For CRCM–BATS-R-US run, we have found that potential drops at low latitudes are diminished by approximately a factor of two compared with the zero-shielding case. Therefore, even relatively weak shielding significantly reduces the effect of isolated substorm injection.

[41] An injection contribution to the RC can also be seen from pressure profiles. Figure 5a shows a radial profile of total pressure at t = 2.5 h, along MLT = 0000 at the end of a period of stationary strong convection, for FokRC–BATS-R-US, CRCM–BATS-R-US and BATS-R-US stand-alone (uncoupled) runs. Figure 5b shows the profiles after the injection occurs, at t = 6.5 h.

[42] Before the injection, the profiles for CRCM–BATS-R-US and FokRC–BATS-R-US runs are comparable. In the BATS-R-US run, the pressure is an order of magnitude lower than for runs with an inner magnetosphere model. The maximum value for both runs with RC is ~10 nPa. For the BATS-R-US run, the value of the pressure in the inner magnetosphere is ~0.5 nPa. This result is consistent with that obtained by *Toffoletto et al.* [2004] and *De Zeeuw et al.* [2004]. After the injection, the pressure radial profiles change dramatically. The maximum value of the pressure for the CRCM–BATS-R-US run is ~30 nPa. The maximum is located at r ~4.2 R_E. The maximum value of pressure for the FokRC–BATS-R-US run is significantly higher, ~110 nPa; the maximum is located at ~3.5 R_E. This demonstrates the importance of ionospheric feedback in RC models. Statistical studies of pressure profiles in the inner magnetosphere are in good agreement with CRCM–BATS-R-US results and show that the value for the pressure peak is ~10–30 nPa [*Lui*, 2003; *Ebihara et al.*, 2002].

[43] It is important to note that Dst* changes the behavior from increasing to decreasing shortly (several minutes) after the dipolarization starts (t = 5.3 h, Figure 1). This is a consequence of global change in magnetospheric dynamics and affects both the preexisting ring current and newly injected one.

3.3. Ring Current Pressure and Electric Field Dynamics

[44] Figure 6 shows the dynamics of the inner magnetosphere over several snapshots during the idealized event for the CRCM–BATS-R-US run. For each selected time, a plot of total RC pressure and a plot of field-aligned current are shown. All quantities are mapped to the equatorial plane. The plot of field-aligned currents is overlayed with equipotentials for the convection electric field (without corotation).

3.3.1. Steady Convection at Southward Bz and SAID/PJ Signature

[45] Near the beginning of the run at t = 0.77 h, the RC is weak and concentrated around midnight. The Region II

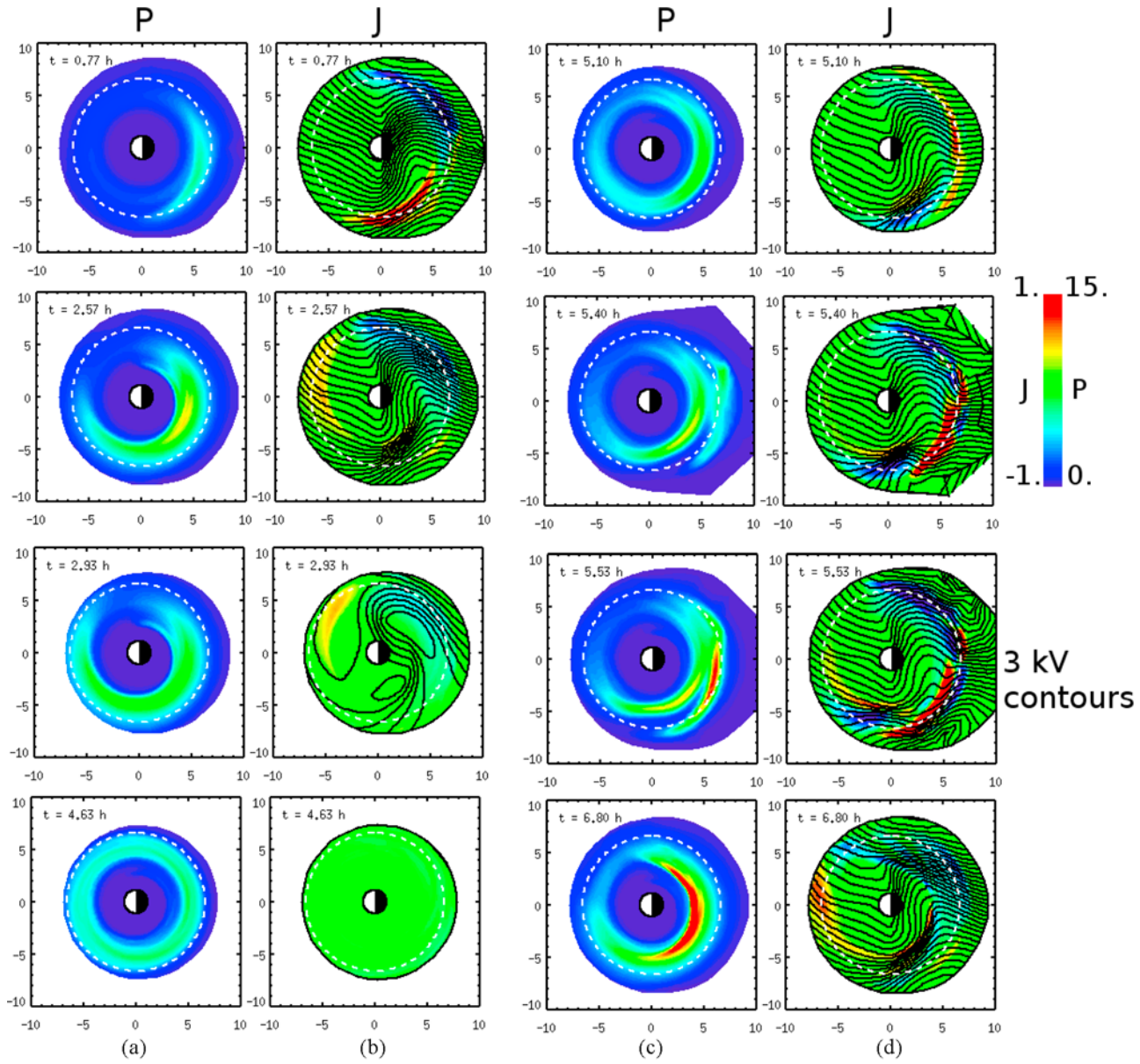

Figure 6. Ring current dynamics for the CRCM–BATS-R-US idealized event. (a and c) Ring current (RC) pressure for 1–180 H^+ (in color, logarithmic scale) at different times, t. (b and d) Snapshots of ionospheric Birkeland currents (BC) for the same times (in color) overplotted with convection equipotentials; corotation is excluded. All quantities are mapped onto the equatorial plane. BC and RC pressure are in $\mu A/m^2$ (from −1 to +1) and nPa (from 0 to 15), respectively. Equipotentials are 3 kV spacing. BC are positive down into the ionosphere. Sun is to the left. Dashed circles denote geostationary orbit.

current is clearly seen in Figure 6 as an upward field-aligned current (blue color) in the dawn sector and a downward field-aligned current (red color) in the dusk sector. However the shielding is weak because field-aligned currents are located in a zone with relatively high conductivity (not shown here).

[46] At the end of the Bz southward interval (t = 2.57 h), the RC is strongly asymmetric. There is a band of enhanced electric field in the dusk sector (MLT ~2000 h) which can be associated with a Subauroral Ion Drift/Polarization Jet signature (SAID/PJ) [*Galperin et al.*, 1974; *Spiro et al.*, 1978]. SAID/PJ fields are usually associated with a newly injected plasma sheet population due to the strong convection [e.g., *Toffoletto et al.*, 2003]. This feature is seen in the dusk sector (MLT ~2000 h). It is formed after ~1 h of simulations and can be interpreted as a result of shielding from enhanced electric field [*Southwood and Wolf*, 1978]. Shielding is also manifested by the skewing of the equipotential lines in the morning sector [*Brandt et al.*, 2002; *Wolf et al.*, 2007]. The Region II current is extended to the dayside sector, but due to high conductivity the effect on the electric field is weak.

3.3.2. Overshielding After Bz Turning and Formation of Symmetric Ring Current at Northward Bz

[47] At t = 2.93 h the polar cap potential drops substantially, and the RC-imposed electric field becomes apparent. This effect is seen as a two-cell convection pattern with one cell centered around MLT ~0300 h and the other cell around MLT ~1900 h. This is an overshielding effect. Because the polar cap potential does not drop simultaneously, the RC has time to adjust itself to a more symmetric configuration, so the overshielding is not as strong as in the case of a simultaneous potential drop. At t = 4.64, the end of the northward Bz interval, the RC becomes symmetric, as expected, and the RC-imposed electric field is almost zero.

3.3.3. Substorm Growth Phase and Dipolarization/ Injection

[48] At t = 4.7 h, the potential drop begins to increase and the RC becomes asymmetric again. As a result, a strong longitudinal pressure gradient and field-aligned current arises at t = 5.1 h. In the dusk sector (MLT ~2000 h), field-aligned currents trigger an appearance of strong electric fields that resemble that of a SAID/PJ. This structure intensifies in the end of the growth phase. The Dst* changes little, thus this is an effect of RC reconfiguration. The pressure gradients are formed by the preexisting population, so the time of formation is short, about ~15 min after the potential drop starts to increase.

[49] Field-line stretching on the nightside begins at t = 4.7 h and lasts until the reconnection occurs at t = 5.3 h and dipolarization develops. Before the dipolarization starts, the induction electric field on the nightside worked against convection and particle transport into the inner magnetosphere. After the dipolarization starts, a strong convection together with induction electric field pushes particles into the inner magnetosphere and creates an injection. The injection is concentrated on the nightside and makes a quadrupole structure of field-aligned currents (t = 5.4, 5.53 h).

[50] This complex structure of field-aligned currents is well explained in terms of Vasyliunas equation for isotropic pitch angle distribution:

$$J = \frac{B_i}{2B}\hat{b} \cdot \nabla P \times \nabla V$$

[*Vasyliunas*, 1970] where J is field-aligned current calculated in the ionosphere, B_i is an ionospheric magnetic field, P is a plasma pressure, V is volume of magnetic flux tube. For simplicity, we use here the isotropic form of the Vasyliunas equation, although field-aligned currents in the model are calculated from its kinetic version, as described in Appendix C. To understand how the structure of field-aligned currents is formed, the isotropic form is sufficient. Because the radial component of E × B drift (combined effect of induction electric field and convection) is larger around midnight, particles intrude into the inner magnetosphere more deeply near midnight. This creates an angle between ∇P and ∇V at polar and equatorial edges of the injection region. The sign of the cross product is changed during transition from premidnight to postmidnight sector. Additionally, the direction of ∇P is opposite at polar and equatorward edges. As a result, a pair of field-aligned currents is formed both at the inner (equatorward) edge of the injection and at the outer (polar) edge.

[51] At t = 5.53 h, two populations persist: a preexisting one, and a newly injected population. Each population is spatially confined, and carries two layers of field-aligned current. This layered structure is clearly seen in the dusk sector and interlaced in the dawn sector where the two populations coexist. There are two separated signatures of SAID/PJ in the dusk sector: one of them corresponds to the old population and the second corresponds to newly injected population. The injection-induced SAID/PJ forms between t = 5.4 h and t = 5.53 (~8 min).

[52] Gradually the new population merges with the old one. At t = 6.8 h a new quasi-stationary picture is established, similar to that at t = 2.5 h before the southward-northward Bz turning, with quasi-stationary SAID/PJ, shielding and Region II currents.

[53] The SAID/PJ signature that arises at the substorm growth phase is more localized at MLT then that of quasi-stationary SAID/PJ under a strong stable convection. Also, this structure is transient and eventually merges with the SAID/PJ near the injection region, forming the quasi-stationary SAID/PJ during substorm recovery phase.

[54] In the FokRC–BATS-R-US run, the development of the injection is similar to that in CRCM–BATS-R-US model, but completely missing the structure of electric fields and Region II field-aligned currents (Figure 7). The electric field structure for the FokRC–BATS-R-US run remains the same all the time (modified by scaling factor from the CPCP). Due to an artificially placed boundary at low latitudes in the FokRC-BATS-R-US model, there are also two regions of extremely high electric field in the dusk and dawn sectors near the equatorial boundary. This electric field arises because boundary condition for MHD ionospheric solver assumes zero electric field at latitudes below 50.7°. Equipotential lines are expelled from the region equatorward of the boundary, creating an enhanced electric field. The intensive electric field together with lack of shielding pushes particles closer to the Earth and creates significantly higher RC pressure than in the case of self-consistent electric field with the shielding (Figure 5).

4. Results for 12 August 2000 Event

[55] The geomagnetic storm on 12 August 2000 occurred on the third day of a period of intense geomagnetic activity which started on 10 August 2000. During 10–11 August 2000, a number of sawtooth events were reported [*Henderson et al.*, 2006], with Dst minimum ~−106 nT at ~0700 UT, 11 August 2000. Early on 12 August 2000 (0000–0200 UT), the activity was relatively small (Figure 8). At ~0215 UT, a strongly southward Bz arrived at the magnetopause and caused the development of a large substorm (as seen in AL index) at ~0300 UT. Dst/SYMH indices reach the minimum of ~−235 nT at ~1000 UT. Figure 8a shows ACE SW bulk velocity and density for that interval acquired by the Advanced Composition Explorer (ACE). Figure 8b shows GSM Bz and By IMF components. All data are shifted to bow shock position. Figure 8c shows AU/AL indices, and Figure 8d shows SYMH/Dst indices.

[56] The BATS-R-US run begins at 1800 UT, 11 August 2000, and ends at 1200 UT, 12 August 2000. The output is saved every 4 min at 1800 UT < t < 0200 UT; 0630 UT < t < 1200 UT and 2 min at 0200 UT < t < 0630 UT, near the

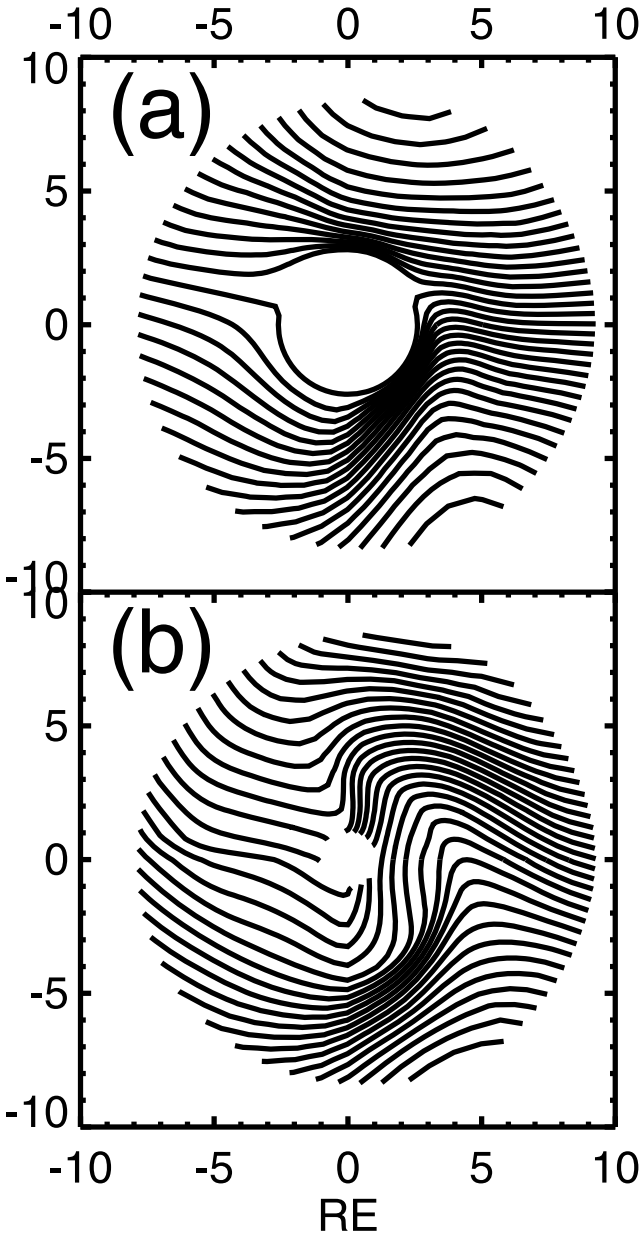

Figure 7. Comparison of electric potential for (a) FokRC-BATS-R-US and (b) CRCM–BATS-R-US idealized event, t = 2.7 h. Equipotentials are 3 kV spacing. Sun is to the left.

main phase. CRCM–BATS-R-US and FokRC–BATS-R-US runs begin at 1830 UT. To obtain density and temperature for CRCM/FokRC input we double MHD density and diminish the temperature by factor two at the polar CRCM/FokRC boundary, keeping the pressure constant.

[57] To justify the factor two, we plot the adjusted BATS-R-US density and temperature and compare with one obtained from *Tsyganenko and Mukai* [2003] empirical model of the plasma sheet (Figure 9). The MHD density and temperature are taken at the polar CRCM/FokRC boundary (~8 R_E) near the midnight. The Tsyganenko and Mukai model is calculated near 10 R_E at the midnight. The SW and IMF data for Tsyganenko and Mukai model are averaged over 20 min. The BATS-R-US temperature and density after adjustment by factor two are in reasonable agreement with the empirical model. Also, we have found that high value for the temperature at the RC boundary in the original setup (with nonadjusted MHD parameters) reduces ENAs fluxes in the postmidnight RC enhancement. The adjustment makes the data-model comparison with IMAGE/HENA better.

[58] A high value for the temperature at the boundary probably indicates a lack of two-way coupling that makes field lines more stretched and the ratio density/temperature more reasonable (results for RCM–BATS-R-US two-way coupled model were taken from CCMC Web site; not shown here).

4.1. Cross Polar Cap Potential: MHD Versus Empirical Models

[59] Figure 10a shows the MHD CPCP calculated for both northern and southern hemispheres and the potential drop along polar boundary in FokRC/CRCM runs. There is an apparent difference between the CPCP in two hemispheres. At the end of the run, this difference is about a factor of two. There are several reasons that explain this effect. The first reason is a different geometry of an open magnetic field lines due to the tilt angle and effect of large By (~30 nT). The other reason is a difference in the illumination by the sunlight, and hence in the conductivities between two hemispheres [e.g., *Zhang et al.*, 2007]. Besides these factors, it is possible that some numerical errors related to finite grid resolution and numerical diffusion contribute to the differ-

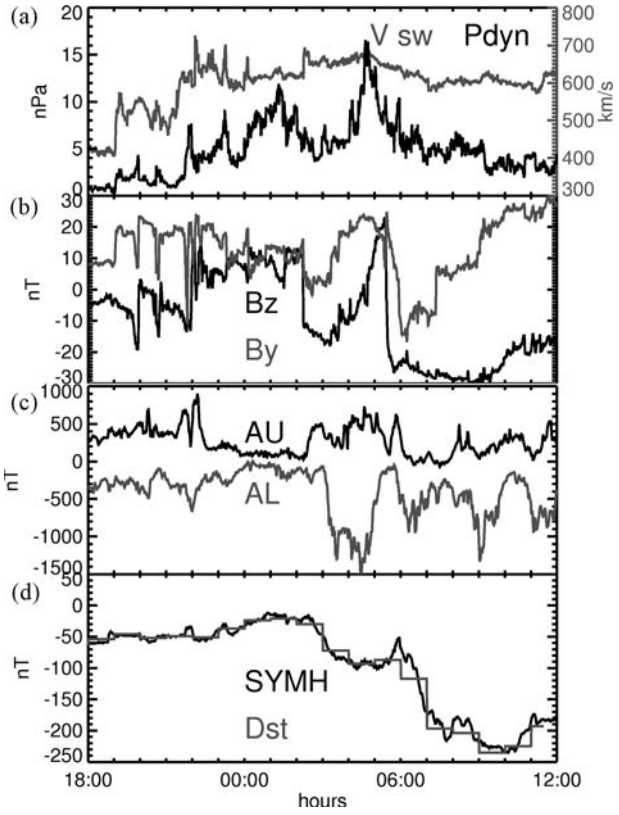

Figure 8. Geomagnetic conditions for 11–12 August 2000. (a) Solar wind P_{dyn} and velocity (OMNIweb); (b) IMF Bz and By (OMIweb); (c) AU and AL (Kyoto); (d) SYMH and Dst (Kyoto).

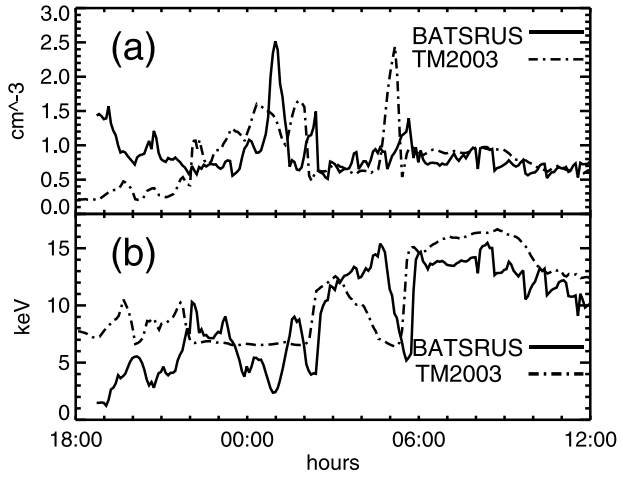

Figure 9. Comparison of adjusted BATS-R-US plasma parameters at the polar CRCM/FokRC boundary with the Tsyganenko and Mukai (TM2003) plasma sheet model for 11–12 August 2000. (a) BATS-R-US adjusted density (doubled by factor two) and TM2003 density; (b) BATS-R-US adjusted temperature (diminished by factor two) and TM2003 temperature. The BATS-R-US plasma parameters are taken from ~8 R_E near geomagnetic equator at the midnight. TM2003 is calculated at the midnight at 10 R_E with SW and IMF data averaged over 20 min.

ence in CPCP on the open field lines. It is difficult to estimate this effect here. The dependence of cross polar cap potential and potential drop along field line may be studied by varying grid resolution and the MHD solver and will be a subject of future work.

[60] Figure 10b shows CPCP calculated from three models which are used as an input to CRCM: Boyle relation [*Boyle et al.*, 1997], Hill-Ober relation [*Ober et al.*, 2003] and Weimer-2000 model [*Weimer*, 2001] for northern ionosphere. To calculate the potential value, SW and IMF data were averaged over the interval of 1 min and shifted to bow shock position. There is a remarkably good correlation between MHD potential and the one calculated from the other models, with the best agreement found with the Weimer-2000 model. The Boyle relation overestimates CPCP for large Bz and By, because it does not include CPCP saturation. It should be noted that the Boyle relation does not include also any dependence from conductivity or tilt angle. In other words the CPCP calculated from the Boyle relation is the same for two hemispheres and cannot describe any seasonal dependence of CPCP or difference between two hemispheres. The Hill-Ober relation includes the dependence from conductivity in the polar cap but not from tilt angle. Even in the case of symmetric conductivities, with the tilt angle the geometry of open/closed lines will be different in the two hemispheres.

[61] Figure 10c shows AMIE-derived 1 min CPCP [*Ridley and Kihn*, 2004] overlapped with BATS-R-US CPCP from Figure 10a. The comparison is reasonable, so at least for this particular case AMIE data, MHD results and empirical models are in good agreement.

[62] Note also the relatively sharp spikes in BATS-R-US CPCP (Figure 10a) are reproduced by three empirical models (Figure 10b). Almost each spike in Figure 10b during 1900–0100 UT has a corresponding spike in Figure 10a, and some of them are also seen in AMIE CPCP. The detailed analysis of BATS-R-US CPCP, AMIE-derived CPCP and Weimer-2000 CPCP shows that BATS-R-US CPCP can resolve sharp changes in 1 min averaged SW data (as seen by Weimer-2000 model) with 5 min accuracy. This is some justification that empirical models for ionospheric potential which depend from current SW and IMF conditions can be used under varying SW and IMF input, when the SW and IMF data are properly averages and shifted in time to bow shock position. The averaging time can be model-dependent.

[63] It has been shown for an idealized case (section 3.1) that the MHD quasi-stationary state in CPCP is achieved after ~15 min. The difference between the reaction time for the idealized case and the real case is explained by at least two factors. First, the overall driving for the real case is stronger. For example, the delay time between arrival of strong southward SW Bz at ~0535 UT to the bow shock (at ~10 R_E) and buildup of strong convection in the ionosphere is ~2 min. The second reason is that the quasi-stationary state is not reached in a real case if the variations in SW/IMF conditions are faster then the reaction time for an idealized case (with instant SW and IMF conditions).

4.2. Energetic Neutral Atom Images

[64] During the main phase of 12 August 2000 storm the RC exhibited strong MLT asymmetry–postmidnight enhancement of 10–100 keV protons and energetic neutral atom (ENA) fluxes. This feature was successfully modeled by CRCM [*Ebihara and Fok*, 2004] for several storms and for 12 August 2000 storm particularly. It was concluded that

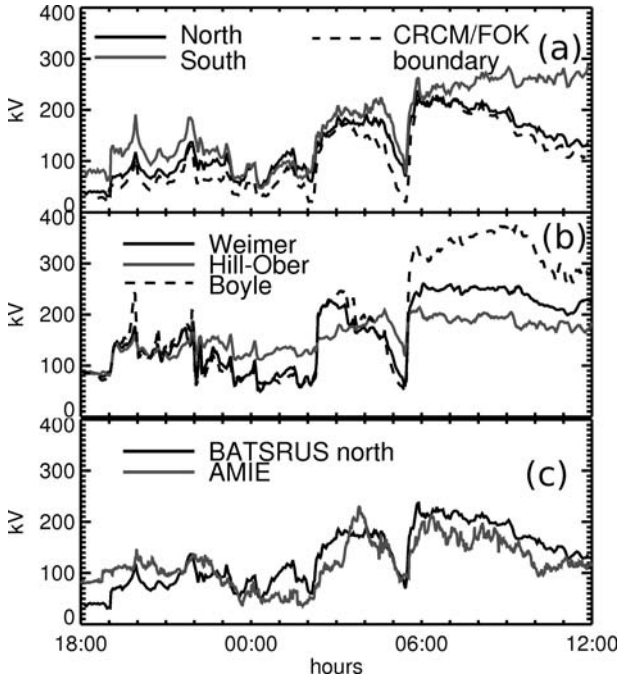

Figure 10. CPCP dynamics during 11–12 August 2000. (a) CPCP for BATS-R-US in northern and southern hemispheres and at CRCM/FokRC polar boundary; (b) CPCP for Boyle, Weimer, and Hill-Ober models; (c) AMIE-derived CPCP and BATS-R-US CPCP for northern hemisphere.

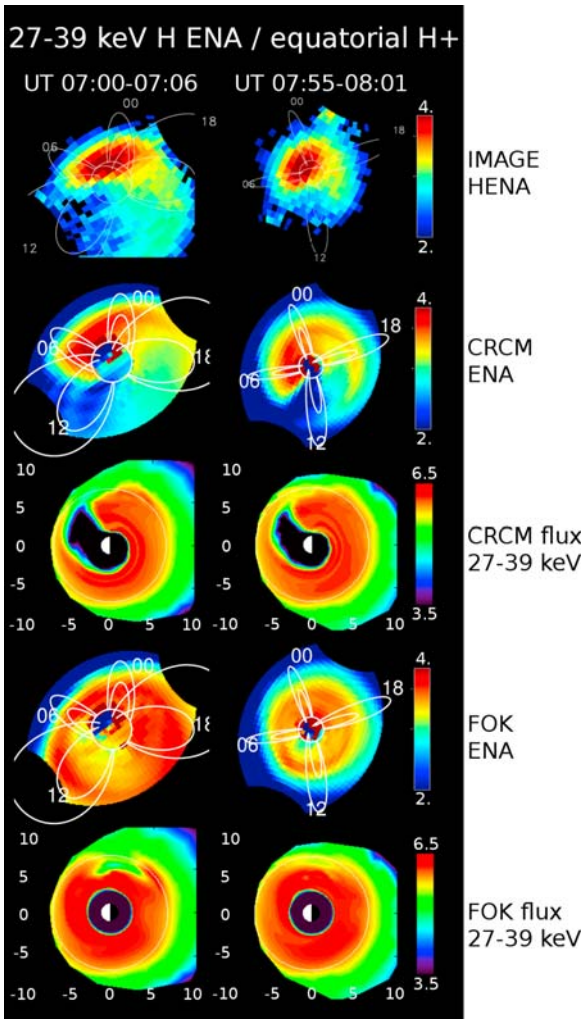

Figure 11. The postmidnight enhancement of the ring current during the main phase of the 12 August 2000 storm at (left) 0700 UT and (right) 0800 UT. (top to bottom) IMAGE/HENA 27–39 keV H ENA flux (/sm^2/sr/s); CRCM–BATS-R-US simulated H ENA flux (/sm^2/sr/s); CRCM–BATS-R-US equatorial differential 27–39 keV H$^+$ flux (/keV/sm^2/sr/); FokRC–BATS-R-US simulated H ENA flux; FokRC–BATS-R-US equatorial differential 27–39 keV H$^+$ flux. A logarithmic scale is used.

this is very natural behavior of RC ions and is explained by the combined effect of electric field shielding and the sharp conductivity gradient near the terminator. By modeling of ENA emissions and comparing with IMAGE/HENA data, we check the validity of CRCM–BATS-R-US and FokRC–BATS-R-US models.

[65] We consider ENA emissions from RC as optically thin. In this case ENA intensity can be obtained from line of sight integrals [*Roelof*, 1987]: $j_{ENA,s} = \sigma_s \int n_H j_s dr$, where σ_s is charge-exchange cross section; n_H – geocorona H density, j_s is the ion (H$^+$ or O$^+$) intensity. The details of the ENA calculations are given by *Ebihara and Fok* [2004].

[66] Figure 11 shows the IMAGE/HENA data at two snapshots during the main phase of the storm (at t = 0700 UT and t = 0800 UT) together with modeled ENA emissions and equatorial differential H$^+$ flux for FokRC–BATS-R-US and CRCM–BATS-R-US runs. Figure 11 shows IMAGE/HENA flux integrated in the energy range 27–39 keV. Strong emissions between MLT 0000 and 0600 h with a taillike structure in the evening sector is a clear example of postmidnight RC enhancement at the storm's main phase [*Brandt et al.*, 2002; *Ebihara and Fok*, 2004]. The CRCM–BATS-R-US modeled emissions (Figure 11) show a good agreement with the data, both in spatial distribution and intensity. RC ENA emissions shown here are a reasonably good representation of the local time distribution of the underlying ring current ion distribution which has clear enhancement in the postmidnight sector and tail in the evening sector.

[67] The modeled ENAs (Figure 11) for the FokRC–BATS-R-US run are completely different from the HENA data in terms of spatial distribution. The reason for this discrepancy is the effect of ionospheric feedback and shielding effects of RC-imposed electric field. In the absence of shielding (FokRC–BATS-R-US run), induction electric field pushes particles closer to the Earth. After some time the RC becomes more symmetric (Figure 11). ENAs are "reflected" from the symmetric RC and form a ring around the Earth.

[68] The overestimation of fluxes by FokRC–BATS-R-US is also seen from comparison of modeled SYMH* with pressure-corrected Kyoto SYMH index (Figure 12). There is a good agreement between CRCM–BATS-R-US and corrected SYMH. FokRC–BATS-R-US SYMH* shows qualitatively the same behavior but the absolute value is considerably larger both for CRCM–BATS-R-US SYMH* and Kyoto SYMH*.

[69] It should be noted that optically thick low-altitude emissions from the exosphere are not modeled properly here. We can only estimate a possible location of such an emissions by including an exospheric oxygen component in the ENA calculations. From the modeled ENA images, these emissions can be seen as dark red pixels near the Earth's limb. These pixels probably correspond to low-altitude emission in the data. More precise calculations of low-altitude emissions are under the way.

[70] Because ENA production depends from pitch angle distribution, it is interesting to see how large the anisotropy becomes in the inner magnetosphere. Figure 13 shows the anisotropy of CRCM–BATS-R-US equatorial fluxes calculated at 0800 UT at 27–39 H$^+$ keV and 60–120 H$^+$ keV;

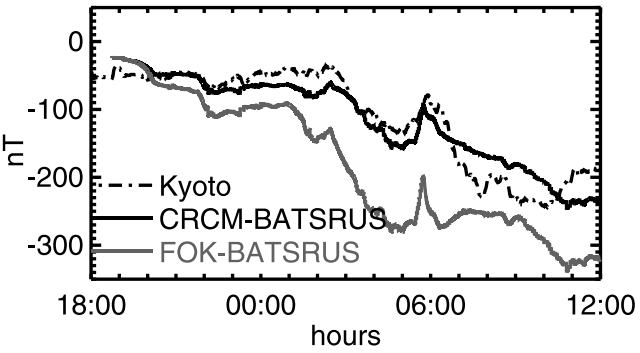

Figure 12. Pressure-corrected Kyoto SYMH, CRCM–BATS-R-US SYMH*, and FokRC–BATS-R-US SYMH* for 11–12 August 2000.

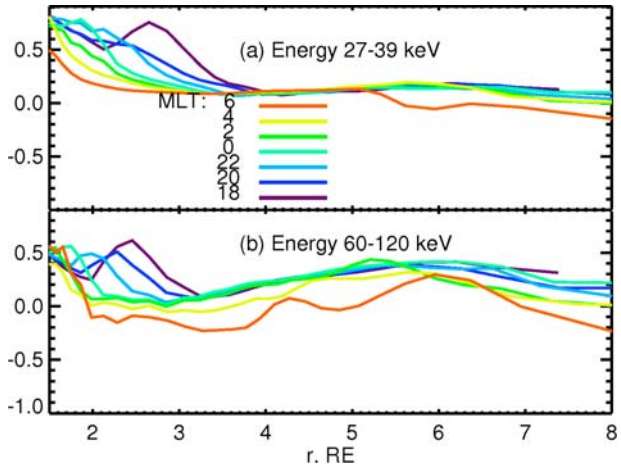

Figure 13. Radial profiles of pitch angle anisotropy for equatorial CRCM–BATS-R-US H^+ flux at 0800 UT, 12 August 2000. (a) Energy range is 27–39 keV; (b) energy range is 60–120 keV. Anisotropy −1/0/1 corresponds to field-aligned/isotropic/perpendicular distribution, respectively. Profiles for different MLT sectors are shown by color.

IMAGE/HENA data at 60–120 keV are not shown here, but integrated ENA flux for this energy range is the same order of magnitude as integrated ENA flux at 27–39 keV. Anisotropy is defined as $A = (j_{perp} - j_{par})/(j_{perp} + j_{par})$, where j_{perp} and j_{par} are perpendicular and parallel flux, respectively. If $A = 0$ then perpendicular and parallel fluxes are equal in magnitude, i.e., the case of isotropic distribution. The case $A = 1$ corresponds to pure perpendicular distribution, and $A = -1$ to pure parallel distribution. The obtained pitch angle distribution is not isotropic, and isotropy depends on energy, equatorial distance r and MLT. A detailed explanation of the obtained profiles is difficult to make due to time-dependent behavior of the electromagnetic field, although drift shell splitting in the asymmetric magnetic field plays some role, especially for high energies. Most of ENA production is confined within the sphere with $r \sim 3\ R_E$, where geocorona density is high. Pitch angle distribution defines what fraction of distribution function covers this region. In general, field-aligned distribution would produce stronger ENAs then that of isotropic (with the same number of particles in magnetic flux tube), and isotropic distribution would produce more strong ENAs then that of equatorial. The dependence of ENA production from pitch angle distribution is studied by *Zheng et al.* [2008].

[71] CRCM–BATS-R-US model can describe not only global RC morphology but also RC injections. An example is shown in Figure 14 which shows integrated HENA flux for energies in the range of 60–119 keV at 0230 UT. The first image is taken at 0230 UT, after the Bz turning at 0215 UT. At this time both modeled and observed SYMH* starts to decrease indicating the RC buildup. The next two images are taken at 0254–0258 UT and 0308–0312 UT accordingly. Low-altitude emissions are intensified at ~0256 UT. Additionally, a strip of enhanced ENA flux is seen in nightside sector. This strip appears at ~0256 UT and becomes brighter at ~0310 UT. At the same time IMAGE/HENA data show significant intensification of low-altitude emissions in the conjugate hemispheres.

[72] Figure 14 shows modeled ENA emissions for the CRCM–BATS-R-US simulation. Both low-altitude emissions (as dark red pixels near the Earth) and strip in the nightside sector are seen. At ~0256 UT, there is an intensification of the emissions corresponding to the same feature in the data. From equatorial fluxes, it is seen that the enhancement in ENA emissions corresponds to enhancement in equatorial fluxes. In other words, the rapid southward Bz turning at 0215 UT causes RC buildup and intensification of 60–119 keV H^+ fluxes in the inner magnetosphere, which is seen from ENA data. The agreement is better for the CRCM–BATS-R-US model. Again, FokRC–BATS-R-US demonstrates significantly higher fluxes both for ENA and equatorial H^+ fluxes than for CRCM–BATS-R-US.

[73] To analyze the relation between ENA/H^+ enhancement and substorm activity we have plotted GOES 8/10 magnetic field tilt angle, AU/AL indices, CRCM–BATS-R-US calculated SYMH* index and pressure-corrected Kyoto SYMH (Figure 15). At ~0230 UT, shortly after Bz changed polarity at ~0215 UT, GOES shows stretching of magnetic field lines. This can be identified as the substorm growth phase. GOES 8 and GOES 10 detect a dipolarization at ~0300 UT (MLT ~2200 h) and ~0310 UT (MLT ~1800 h) accordingly. The start of dipolarization at GOES 8 coincides with a sharp AL intensification and may be attributed to substorm expansion onset. However, modeled SYMH* and pressure-corrected Kyoto SYMH indices show that RC buildup has started before the substorm onset. Analysis of BATS-R-US magnetic field configuration shows that there is no dipolarization signature at geostationary orbit between 0200 and 0400 UT (not shown here). Analysis of IMAGE/HENA fluxes near 0300 UT does not show significant temporal changes in RC emissions, although there is an intensification of low-altitude emissions at that time. We conclude that both the RC buildup (SYMH index) and the RC injection signature from IMAGE/HENA data are the result of enhanced convection during the substorm growth phase. We do not consider low-altitude emissions here. Good quality IMAGE/HENA data are available until ~0315 UT, so there is some possibility that the substorm may influence RC ENA emissions later.

[74] We have found that Dst*/SYMH* has been decreased during the substorm growth phase. The result is different from what we obtained in section 3.2, where Dst*/SYMH* increased during the substorm growth phase. This is explained by the difference in the convection strength: modeled CPCP is ~100 kV for the idealized event and ~200 kV for 0230 UT of 12 August 2000.

5. Summary and Conclusions

[75] We present the first results of a new CRCM–BATS-R-US model combination and compare them with those of the FokRC–BATS-R-US model combination. Both models take SW and IMF data as an input and produce ring current (RC) particle fluxes in the inner magnetosphere as an output; however, CRCM–BATS-R-US considers a more realistic magnetosphere-ionosphere coupling. The difference between two models is that the FokRC takes the electric field from the MHD code while the CRCM calculates the electric field in a self-consistent way and MHD electric potential is used only as a polar boundary condition.

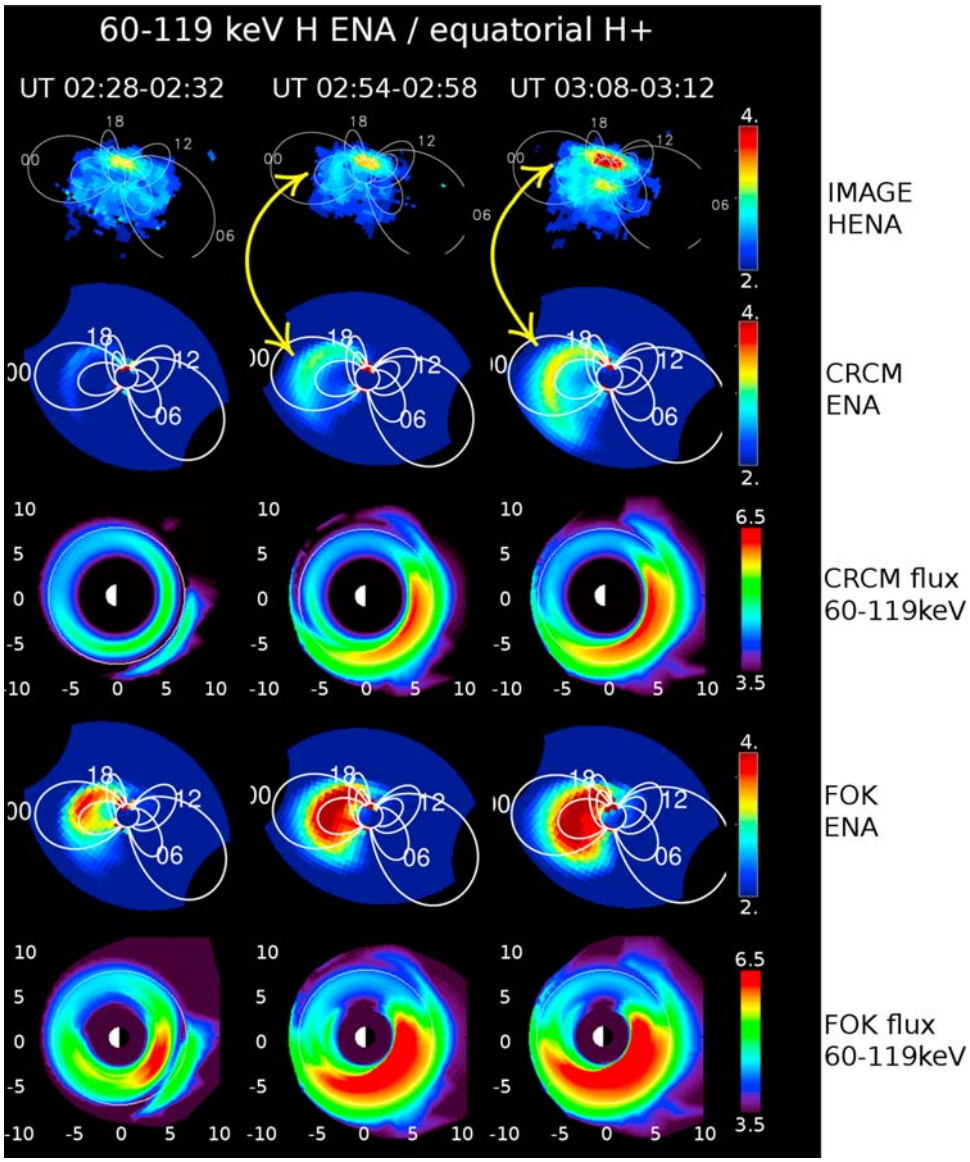

Figure 14. The development of a ring current injection during the 12 August 2000 storm. (top to bottom) IMAGE/HENA 60–119 keV H ENA flux (/sm^2/sr/s); CRCM–BATS-R-US simulated H ENA flux (/sm^2/sr/s); equatorial differential 60–119 keV H^+ flux (/keV/sm^2/sr/s); FokRC–BATS-R-US simulated H ENA flux; FokRC–BATS-R-US equatorial differential 60–119 keV H^+ flux. The scale is logarithmic. At ~0215 UT, a southward Bz turning triggers activity. (left) At UT 0230, H^+ fluxes and H ENAs before the development of the injection. (middle) At 0255 UT, particles intrude deeply into the inner magnetosphere in the evening sector. This causes an intensification of ring current ENA emissions both in IMAGE/HENA data and in simulated results. (right) 0310 UT.

[76] The comparison of CRCM–BATS-R-US with FokRC–BATS-R-US results show that realistic coupling with the ionosphere (effect of RC-imposed electric field) plays a key role in the electrodynamics of the inner magnetosphere. The lack of a RC-imposed electric field in FokRC–BATS-R-US causes significantly higher particle fluxes and pressure in the inner magnetosphere then that of CRCM–BATS-R-US. This result is consistent with the result of *Taktakishvili et al.* [2007b] who found that FokRC–BATS-R-US produces fluxes at the geosynchronous orbit which are significantly higher then LANL data (Figure 2 from *Taktakishvili et al.* [2007b]).

[77] The CRCM–BATS-R-US model can successfully reproduce the postmidnight RC enhancement as seen by IMAGE/HENA on 12 August 2000 during the late main phase of the storm. During the early main phase, we extract a ring current injection signature from IMAGE/HENA data. The CRCM–BATS-R-US model can successfully reproduce this injection (high-altitude RC ENA emissions). The analysis of SYMH, AL indices, GOES data and model results leads to the suggestion that this injection is due to enhanced convection during the substorm growth phase at the beginning of the storm's main phase. For the FokRC–BATS-R-US model, agreement with IMAGE/HENA is

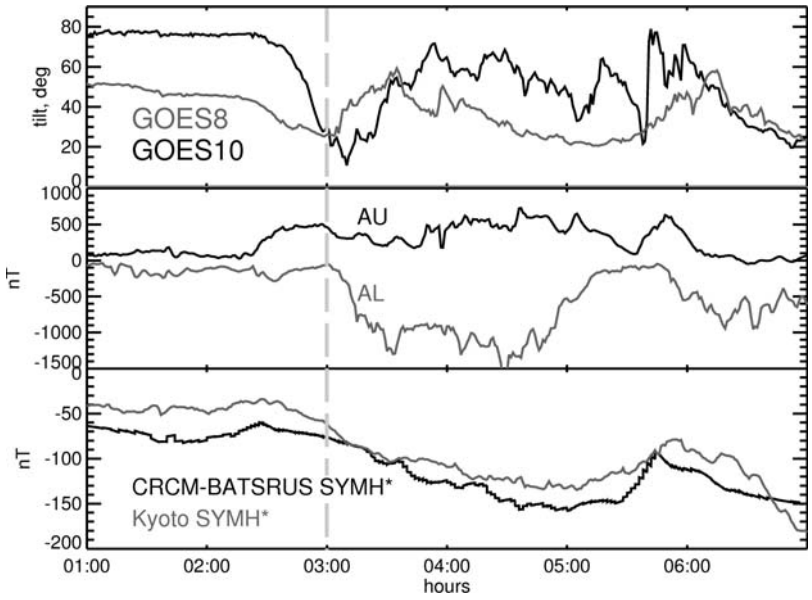

Figure 15. Close-up view of the main phase. (top to bottom) GOES 8 and 10 magnetic field tilt (CDAWeb); AU and AL indices (Kyoto); CRCM–BATS-R-US SYMH* and pressure-corrected SYMH (Kyoto). The dashed line shows the substorm onset.

poor. Modeled SYMH* is significantly lower than pressure-corrected Kyoto SYMH and CRCM–BATS-R-US SYMH*.

[78] For the idealized event, CRCM–BATS-R-US successfully reproduces well known features of inner magnetosphere electrodynamics: strong convection under the southward Bz; the development of an electric field shielding; an overshielding effect when Bz changes the polarity from southward to northward; a weak convection under prolonged interval of northward Bz; an induction electric field during the substorm development; SAID/PJ electric field in the dusk sector during strong convection. By calculating a potential drop along a given ionospheric latitude, we quantitatively describe the shielding, overshielding and penetration electric field effects and estimate the characteristic lifetimes.

[79] For the idealized case, we have shown that the stable structure of Region II field-aligned currents is formed during prolonged intervals of strong quasi-stationary convection, or at final stage of substorm development. During transient states when Bz changes polarity and/or substorm occurs, multilayered structures of field-aligned currents are formed. We interpret these as complex structures of partial ring current (including injections), created by spatial and temporal variations of electric fields (both convection and induction), and plasma sheet source at polar boundary of ring current model. Our results are consistent with the recent studies of *Yang et al.* [2008], *Buzulukova et al.* [2008], and *Ebihara et al.* [2009] showing that complex structure of Region II currents and RC obtained with RCM and CRCM agrees reasonably well with the observations.

[80] The CRCM–BATS-R-US model shows that SAID/PJs are formed during quasi-stationary strong convection under southward Bz and correspond to quasi-stationary structures of Region II currents. Additionally, strong electric fields in the evening sector, which resemble SAID/PJs appear at a substorm growth phase. This effect occurs when the RC changes configuration from symmetric to asymmetric, and newly injected plasma during substorm development is not needed. The formation time for the structure is ~15 min. The structure that resembles SAID/PJ is also formed near the injection region during substorm development. The formation time of injection-induced SAID/PJ is defined by the substorm injection development (~8 min). The obtained complex structure of electric field may explain some experimental observations of fast (~10 min) formation of SAID/PJ during substorm development deep in the inner magnetosphere [*Khalipov et al.*, 2001; *Mishin and Mishin*, 2007].

[81] We have shown that the FokRC–BATS-R-US model produces stronger RC than that of CRCM–BATS-R-US. In other words, MHD electric and magnetic fields and plasma sheet parameters are sufficient to produce strong RC. This is consistent with the results obtained by *Southwood* [1977] who showed that Region II currents can be also generated in an ideal MHD. However, the BATS-R-US stand alone produces weak RC (low total pressure) and weak Region II currents [*Ridley et al.*, 2001]. This can be explained by difficulties for a global MHD model to resolve with good accuracy near-Earth region [*Toffoletto et al.*, 2004]. To our best knowledge, no studies are published to demonstrate that a global MHD model with good spatial resolution in the near-Earth region is able to reproduce the total pressure and Region II currents comparable with those obtained from existing RC models.

[82] We have found that field-aligned currents in the isolated injection have a quadrupole structure. A similar structure of field-aligned currents in the injection region was reported by *Zhang et al.* [2009] using RCM model. The polar edge of the quadrupole structure was attributed to the substorm current wedge and equator edge of the structure to currents of the Region II [*Zhang et al.*, 2009]. These results, together with CRCM–BATS-R-US results, allow us to

conclude that field-aligned currents of an injection may be a part of substorm current wedge. Recent studies of substorm ground-based signatures and Harang reversal also confirmed the close connection between substorm development and Region II currents [*Zou et al.*, 2009].

[83] However, a self-consistent representation of substorm development, ring current injection and substorm current wedge should include a two-way coupled model, with pressure and electromagnetic feedback from RC model to MHD model. An important part of any two-way coupled model is a calculation of ionospheric conductivities in the Region II self-consistently with electron precipitation and inclusion of ionosphere outflow source as a source of ring current plasma. These model improvements will be a subject for the future work.

Appendix A: BATS-R-US MHD Model

[84] The Block-Adaptive-Tree Solar-Wind Roe-Type Upwind Scheme (BATS-R-US) MHD model solves the governing equations of ideal magnetohydrodynamics:

$$\frac{\partial \rho}{\partial t} + \mathbf{u} \cdot \nabla \rho + \rho \nabla \cdot \mathbf{u} = \mathbf{0} \tag{A1}$$

$$\rho \frac{\partial \mathbf{u}}{\partial t} + \rho \mathbf{u} \cdot \nabla \mathbf{u} + \nabla \mathbf{p} - \mathbf{j} \times \mathbf{B} = \mathbf{0}, \tag{A2}$$

$$\frac{\partial p}{\partial t} + \mathbf{u} \cdot \nabla \mathbf{p} + \gamma \mathbf{p} \nabla \cdot \mathbf{u} = \mathbf{0}, \tag{A3}$$

$$\mathbf{j} = \frac{1}{\mu_0} \nabla \times \mathbf{B}, \tag{A4}$$

$$\frac{\partial \mathbf{B}}{\partial t} + \nabla \times \mathbf{E} = \mathbf{0}, \tag{A5}$$

$$\mathbf{E} = -\mathbf{u} \times \mathbf{B}, \tag{A6}$$

These are the continuity, momentum and heat balance equations together with Faraday's law, Ampere's law and Ohm's law with zero resistivity. In BATS-R-US, these equations are rewritten in conservative form for the eight-dimensional vector **U**:

$$\frac{\partial \mathbf{U}}{\partial t} + (\nabla \cdot \mathbf{F})^{\mathbf{T}} = \mathbf{S}, \tag{A7}$$

where $\mathbf{U} = [\rho, \rho\mathbf{u}, \mathbf{B}, \epsilon]^{\mathbf{T}}$ consisting of density, momentum density, total energy density, and magnetic field. The form of flux tensor **F**, source term **S** (which is proportional to $\nabla \cdot \mathbf{B}$) and the derivation of conservative form of MHD equations can be found in the work of *Powell et al.* [1999].

[85] To resolve regions with strong spatial gradients, BATS-R-US uses a block-adaptive scheme that allows it to automatically refine the grid where it is needed most. In general, BATS-R-US obtains solutions across a range of several orders of plasma β. The detailed description of the model and numerical scheme is given by *Powell et al.* [1999] and *Song et al.* [1999, and references therein].

[86] Outer boundary conditions for BATS-R-US are calculated from SW and IMF parameters at the upstream boundary of simulation region at $X_{\mathrm{GSM}} = 33\ R_E$. The inner MHD boundary is located at 2.5 R_E with plasma density n = 28 cm^{-3} and temperature T = 25000 K. At the inner boundary, field-aligned currents are calculated and projected to the ionosphere. Then the Poisson-like equation is solved:

$$\nabla \cdot (-\Sigma \cdot \nabla \Phi) = J_{\parallel i} \sin I, \tag{A8}$$

where $J_{\parallel i}$ is a field-aligned current in the ionosphere, Φ is an electric field potential, Σ is a tensor of ionospheric conductivities (field-line integrated), I is a magnetic field inclination angle. The details of ionosphere module calculations and inner boundary condition are given by *Ridley et al.* [2004]. Also it should be noted that the field-aligned currents which result from this equation consist mainly from Region I currents, and Region II currents are found to be very weak [*Ridley et al.*, 2001].

[87] For this particular study, the BATS-R-US simulations were performed at the Community Coordinated Modeling Center (CCMC), NASA Goddard Space Flight Center. The output from those simulations were used as inputs for the FokRC and CRCM models.

Appendix B: FokRC Ring Current Model

[88] The FokRC model calculates ring current particle fluxes in the inner magnetosphere for energies in the range of ~1–200 keV. FokRC model solves the bounce-averaged Boltzmann equation to obtain temporal evolution of four-dimensional phase space density $\overline{f}_s = \overline{f}_s(\lambda, \phi, M, K)$, specified by two ionospheric coordinates in north hemisphere (invariant latitude λ and magnetic local time ϕ), and two adiabatic invariants (relativistic magnetic moment M and $K = J/\sqrt{8m_0M}$, J is a longitudinal invariant):

$$\frac{\partial \overline{f}_s}{\partial t} + \langle \dot{\lambda} \rangle \frac{\partial \overline{f}_s}{\partial \lambda} + \langle \dot{\phi} \rangle \frac{\partial \overline{f}_s}{\partial \phi} = -\mathrm{v}\sigma_s \langle \mathrm{n_H} \rangle \overline{f}_s - \left(\frac{\overline{f}_s}{0.5\tau_b} \right)_{loss\ cone} \tag{B1}$$

where the operator $\langle \ldots \rangle$ means bounce averaged, v is a particle velocity, σ_s is a cross section for charge-exchange losses with the geocorona, $\mathrm{n_H}$ is a geocorona H density, and τ_b is a bounce period (the last term is calculated only for particles in the loss cone).

[89] The bounce-averaged velocities $\langle \dot{\lambda} \rangle$ and $\langle \dot{\phi} \rangle$ are:

$$\langle \dot{\lambda} \rangle = -\frac{1}{qG} \frac{\partial H}{\partial \phi} \tag{B2}$$

$$\langle \dot{\phi} \rangle = \frac{1}{qG} \frac{\partial H}{\partial \lambda} \tag{B3}$$

$$G = \frac{M_E \sin 2\lambda}{r_i} \tag{B4}$$

with Hamiltonian H given by:

$$H = \sqrt{p^2c^2 + m_0{}^2c^4} + q\Phi - \frac{q\Omega M_E}{2r_i}\cos 2\lambda. \quad \text{(B5)}$$

where M_E is a magnetic moment of Earth's dipole, r_i is the radius from the center of the Earth to the ionospheric boundary (100 km altitude), q is a charge of a particle, Φ is an electric potential, Ω is the corotation angular velocity. To obtain p, for a given K, M, λ, ϕ the following equation is solved numerically to calculate mirror points and B_m:

$$K = \int_{sm}^{sm'} (B_m - B)^{1/2} ds \quad \text{(B6)}$$

then,

$$p^2(\lambda, \phi, M, K) = 2m_0 B_m M \quad \text{(B7)}$$

[90] The initial energy distribution of the RC is calculated from the empirical *Sheldon and Hamilton* [1993] model. The initial pitch angle distribution is considered to be isotropic. The subsequent isotropy and energy distribution are calculated from the drift motion. For a more detailed description of the model, refer to *Fok et al.* [1995] and *Fok and Moore* [1997].

Appendix C: CRCM Model

[91] The CRCM is a combination of two models: the FokRC model and the RCM model. The calculations are performed in two steps. First, the evolution of distribution function at each point is calculated which is due to drift and losses (FokRC model). Then, the field-aligned currents in the ionosphere and ionospheric potential are calculated using RCM scheme (for the details, see *Fok et al.* [2001]).

[92] Field-aligned currents are calculated from a current continuity equation between the magnetosphere and ionosphere:

$$J_{\parallel \mathrm{i}} = \frac{1}{r_i \cos^2 \lambda} \sum_j \left(\frac{\partial \eta_j}{\partial \lambda} \frac{\partial W_j}{\partial \phi} - \frac{\partial \eta_j}{\partial \phi} \frac{\partial W_j}{\partial \lambda} \right) \quad \text{(C1)}$$

where the summation is done at fixed λ, ϕ point and over all M, K points, $J_{\parallel \mathrm{i}}$ is a sum of ionospheric field-aligned current densities for both hemispheres, W_j is the kinetic energy of a particle with given λ, ϕ, M, K (the first term in right side of equation (13)) and η_j is the number of particles per unit magnetic flux (density invariant in terms of RCM) associated with ΔM, ΔK:

$$\eta_j = 4\sqrt{2}\pi m_0^{3/2} \overline{f}_s(\lambda, \phi, M, K) M^{1/2} \Delta M \Delta K. \quad \text{(C2)}$$

Using the distribution of field-aligned currents, the ionospheric potential is obtained from equation (8). We assume here that B_i is the same for both hemispheres. By definition, $J_{\parallel \mathrm{i}}$ here describes only Region II field-aligned currents.

Appendix D: Dst*, SYMH* Indices, and DPS Relation

[93] Dst* is estimated from Dessler-Parker-Sckopke (DPS) relation as a linear dependence from the RC energy [*Dessler and Parker*, 1959; *Sckopke*, 1966; *Carovillano and Siscoe*, 1973]: $Dst^* = -\frac{2}{3} B_0 \frac{E_{\mathrm{RC}}}{U_{\mathrm{E}}}$, E_{RC} is a total RC kinetic energy, U_{E} is a total magnetic energy of the Earth's magnetic dipole, B_0 is a equatorial horizontal component of the dipole magnetic field. Substituting the values of physical quantities [e.g., *Carovillano and Siscoe*, 1973], we obtain:

$$Dst^*(nT) = -3.98 \cdot 10^{-30} \cdot E_{\mathrm{RC}}(keV), \quad \text{(D1)}$$

where Dst* is the disturbance of magnetic field at the Earth's center due to the ring current induced magnetic field. This result follows from the virial theorem [*Carovillano and Siscoe*, 1973; *Vasyliunas*, 2006] and is valid for dipole fields, any longitudinal RC configuration, and RC distribution function (neglecting the magnetic energy of the RC itself and the contribution from surface terms).

[94] For the 12 August 2000 simulation analysis we additionally use a high-resolution (in time) version of Dst, SYMH index [*Wanliss and Showalter*, 2006]. The RC energy is recalculated to SYMH* with the same linear relation as for Dst*. To convert SYMH into SYMH*, we calculate the pressure correction which is given for Dst/Dst* by *Gonzalez et al.* [1994]:

$$\mathrm{SYMH^*} = \mathrm{SYMH} - \mathrm{c_1 P_{SW}^{1/2}} + \mathrm{c_2}, \quad \text{(D2)}$$

where P_{SW} is a SW dynamic pressure and c_1, c_2 are empirical coefficients equal 0.2 nT/(eV cm^{-3})$^{1/2}$ and 20 nT accordingly. For the idealized run, SYMH* and Dst* are synonymous.

[95] Usually, it is a common practice for RC models and the CRCM in particular [e.g., *Ebihara et al.*, 2004] to use the DPS relation for estimation of Dst* variation. It is assumed in this approximation that the main part of RC energy is concentrated in the inner magnetosphere where deviations from the dipole field are not critical. The other source for possible errors is the pressure correction to Dst, as shown by *Siscoe et al.* [2005]. The validity analysis of the Dst estimate variation from RC energy is beyond the scope of this work, although it seems that coupled MHD-RC model is a good instrument for that purpose.

[96] **Acknowledgments.** This research was supported by NASA Science Mission Directorate, Heliophysics Division, Heliophysics Guest Investigators Program, under Work Breakdown Structure 955518.02.01.02.57, and by an appointment to the NASA Postdoctoral Program at the Goddard Space Flight Center, administered by Oak Ridge Associated Universities through a contract with NASA. The ACE SW and IMF data were obtained from the GSFC/SPDF OMNIWeb interface at http://omniweb.gsfc.nasa.gov. The Dst, AU, AL, and SYMH indices were provided from the WDC for Geomagnetism, Kyoto. Simulation results for BATS-R-US and Ridley IE module have been provided by the Community Coordinated Modeling Center at Goddard Space Flight Center through their public Runs on Request System (http://ccmc.gsfc.nasa.gov). The CCMC is a multiagency partnership between NASA, AFMC, AFOSR, AFRL, AFWA, NOAA, NSF, and ONR. The BATS-R-US model and Ridley IE solver were developed at Center for Space Environment Modeling, University of Michigan. We are indebted to M. Maddox for providing us with KAMELEON library. N. Buzulukova thanks A. Dorodnitsyn for proofreading of the manuscript. The computer programs to calculate ionospheric electrostatic potential in CRCM were written by S. Sazykin. The authors thank A. Ridley for providing AMIE-derived CPCP.

[97] Zuyin Pu thanks the reviewers for their assistance in evaluating this paper.

References

Borovsky, J. E., M. Hesse, J. Birn, and M. M. Kuznetsova (2008), What determines the reconnection rate at the dayside magnetosphere?, *J. Geophys. Res.*, *113*, A07210, doi:10.1029/2007JA012645.

Boyle, C. B., P. H. Reiff, and M. R. Hairston (1997), Empirical polar cap potentials, *J. Geophys. Res.*, *102*, 111–126, doi:10.1029/96JA01742.

Brandt, P. C., S. Ohtani, D. G. Mitchell, M.-C. Fok, E. C. Roelof, and R. Demajistre (2002), Global ENA observations of the storm mainphase ring current: Implications for skewed electric fields in the inner magnetosphere, *Geophys. Res. Lett.*, *29*(20), 1954, doi:10.1029/2002GL015160.

Buzulukova, N., and V. Vovchenko (2008), Modeling of proton nose structures in the inner magnetosphere with a self-consistent electric field model, *J. Atmos. Sol. Terr. Phys.*, *70*, 503–510, doi:10.1016/j.jastp.2007.08.028.

Buzulukova, N., M.-C. Fok, T. E. Moore, and D. M. Ober (2008), Generation of plasmaspheric undulations, *Geophys. Res. Lett.*, *35*, L13105, doi:10.1029/2008GL034164.

Carovillano, R. L., and G. L. Siscoe (1973), Energy and momentum theorems in magnetospheric processes, *Rev. Geophys.*, *11*, 289–353, doi:10.1029/RG011i002p00289.

Delcourt, D. C., J. A. Sauvaud, and T. E. Moore (1993), Polar wind ion dynamics in the magnetotail, *J. Geophys. Res.*, *98*, 9155–9169, doi:10.1029/93JA00301.

Delcourt, D. C., T. E. Moore, and C. R. Chappell (1994), Contribution of low-energy ionospheric protons to the plasma sheet, *J. Geophys. Res.*, *99*, 5681–5689, doi:10.1029/93JA02770.

Dessler, A. J., and E. N. Parker (1959), Hydromagnetic theory of geomagnetic storms, *J. Geophys. Res.*, *64*, 2239–2252, doi:10.1029/JZ064i012p02239.

De Zeeuw, D. L., S. Sazykin, R. A. Wolf, T. I. Gombosi, A. J. Ridley, and G. Tóth (2004), Coupling of a global MHD code and an inner magnetospheric model: Initial results, *J. Geophys. Res.*, *109*, A12219, doi:10.1029/2003JA010366.

Ebihara, Y., and M. Ejiri (2000), Simulation study on fundamental properties of the storm-time ring current, *J. Geophys. Res.*, *105*, 15,843–15,860, doi:10.1029/1999JA900493.

Ebihara, Y., and M. Ejiri (2003), Numerical simulation of the ring current: Review, *Space Sci. Rev.*, *105*, 377–452, doi:10.1023/A:1023905607888.

Ebihara, Y., and M.-C. Fok (2004), Postmidnight storm-time enhancement of tens-of-keV proton flux, *J. Geophys. Res.*, *109*, A12209, doi:10.1029/2004JA010523.

Ebihara, Y., M. Ejiri, H. Nilsson, I. Sandahl, A. Milillo, M. Grande, J. F. Fennell, and J. L. Roeder (2002), Statistical distribution of the storm-time proton ring current: POLAR measurements, *Geophys. Res. Lett.*, *29*(20), 1969, doi:10.1029/2002GL015430.

Ebihara, Y., M.-C. Fok, R. A. Wolf, T. J. Immel, and T. E. Moore (2004), Influence of ionosphere conductivity on the ring current, *J. Geophys. Res.*, *109*, A08205, doi:10.1029/2003JA010351.

Ebihara, Y., M.-C. Fok, J. B. Blake, and J. F. Fennell (2008), Magnetic coupling of the ring current and the radiation belt, *J. Geophys. Res.*, *113*, A07221, doi:10.1029/2008JA013267.

Ebihara, Y., N. Nishitani, T. Kikuchi, T. Ogawa, K. Hosokawa, M.-C. Fok, and M. F. Thomsen (2009), Dynamical property of storm time subauroral rapid flows as a manifestation of complex structures of the plasma pressure in the inner magnetosphere, *J. Geophys. Res.*, *114*, A01306, doi:10.1029/2008JA013614.

Ejiri, M. (1978), Trajectory traces of charged particles in the magnetosphere, *J. Geophys. Res.*, *83*, 4798–4810, doi:10.1029/JA083iA10p04798.

Fok, M.-C., and T. E. Moore (1997), Ring current modeling in a realistic magnetic field configuration, *Geophys. Res. Lett.*, *24*, 1775–1778, doi:10.1029/97GL01255.

Fok, M.-C., T. E. Moore, J. U. Kozyra, G. C. Ho, and D. C. Hamilton (1995), Three-dimensional ring current decay model, *J. Geophys. Res.*, *100*, 9619–9632, doi:10.1029/94JA03029.

Fok, M.-C., T. E. Moore, and M. E. Greenspan (1996), Ring current development during storm main phase, *J. Geophys. Res.*, *101*, 15,311–15,322, doi:10.1029/96JA01274.

Fok, M.-C., R. A. Wolf, R. W. Spiro, and T. E. Moore (2001), Comprehensive computational model of Earth's ring current, *J. Geophys. Res.*, *106*, 8417–8424, doi:10.1029/2000JA000235.

Fok, M.-C., et al. (2003), Global ENA image simulations, *Space Sci. Rev.*, *109*, 77–103, doi:10.1023/B:SPAC.0000007514.56380.fd.

Fok, M.-C., T. E. Moore, P. C. Brandt, D. C. Delcourt, S. P. Slinker, and J. A. Fedder (2006), Impulsive enhancements of oxygen ions during substorms, *J. Geophys. Res.*, *111*, A10222, doi:10.1029/2006JA011839.

Fontaine, D., M. Blanc, L. Reinhart, and R. Glowinski (1985), Numerical simulations of the magnetospheric convection including the effects of electron precipitation, *J. Geophys. Res.*, *90*, 8343–8360, doi:10.1029/JA090iA09p08343.

Galperin, Y. I., V. N. Ponomarev, and A. G. Zosimova (1974), Plasma convection in polar ionosphere, *Ann. Geophys.*, *30*(1), 1–7.

Gonzalez, W. D., J. A. Joselyn, Y. Kamide, H. W. Kroehl, G. Rostoker, B. T. Tsurutani, and V. M. Vasyliunas (1994), What is a geomagnetic storm?, *J. Geophys. Res.*, *99*, 5771–5792, doi:10.1029/93JA02867.

Goodrich, C. C., J. G. Lyon, M. Wiltberger, R. E. Lopez, and K. Papadopoulos (1998), An overview of the impact of the January 10–11, 1997 magnetic cloud on the magnetosphere via global MHD simulation, *Geophys. Res. Lett.*, *25*, 2537–2540, doi:10.1029/98GL01159.

Goodrich, C. C., T. I. Pulkkinen, J. G. Lyon, and V. G. Merkin (2007), Magnetospheric convection during intermediate driving: Sawtooth events and steady convection intervals as seen in Lyon-Fedder-Mobarry global MHD simulations, *J. Geophys. Res.*, *112*, A08201, doi:10.1029/2006JA012155.

Harel, M., R. A. Wolf, P. H. Reiff, R. W. Spiro, W. J. Burke, F. J. Rich, and M. Smiddy (1981), Quantitative simulation of a magnetospheric substorm. I - Model logic and overview, *J. Geophys. Res.*, *86*, 2217–2241, doi:10.1029/JA086iA04p02217.

Heinemann, M. (1999), Role of collisionless heat flux in magnetospheric convection, *J. Geophys. Res.*, *104*, 28,397, doi:10.1029/1999JA900401.

Heinemann, M., and R. A. Wolf (2001), Relationships of models of the inner magnetosphere to the Rice Convection Model, *J. Geophys. Res.*, *106*, 15,545–15,554, doi:10.1029/2000JA000389. (Correction, *J. Geophys. Res.*, *106*, 29,943–29,944, doi:10.1029/2001JA900150, 2001.)

Henderson, M. G., et al. (2006), Substorms during the 10–11 August 2000 sawtooth event, *J. Geophys. Res.*, *111*, A06206, doi:10.1029/2005JA011366.

Huang, C.-S., S. Sazykin, J. L. Chau, N. Maruyama, and M. C. Kelley (2007), Penetration electric fields: Efficiency and characteristic time scale, *J. Atmos. Sol. Terr. Phys*, *69*, 1135–1146, doi:10.1016/j.jastp.2006.08.016.

Iijima, T., and T. Shibaji (1987), Global characteristics of northward IMF-associated (NBZ) field-aligned currents, *J. Geophys. Res.*, *92*, 2408–2424, doi:10.1029/JA092iA03p02408.

Jaggi, R. K., and R. A. Wolf (1973), Self-consistent calculation of the motion of a sheet of ions in the magnetosphere., *J. Geophys. Res.*, *78*, 2852–2866, doi:10.1029/JA078i016p02852.

Jordanova, V. K., J. U. Kozyra, G. V. Khazanov, A. F. Nagy, C. E. Rasmussen, and M.-C. Fok (1994), A bounce-averaged kinetic model of the ring current ion population, *Geophys. Res. Lett.*, *21*, 2785–2788, doi:10.1029/94GL02695.

Jordanova, V. K., J. U. Kozyra, A. F. Nagy, and G. V. Khazanov (1997), Kinetic model of the ring current-atmosphere interactions, *J. Geophys. Res.*, *102*, 14,279–14,292, doi:10.1029/96JA03699.

Keller, K. A., M.-C. Fok, A. Narock, M. Hesse, L. Rastaetter, M. M. Kuznetsova, T. I. Gombosi, and D. L. DeZeeuw (2005), Effect of multiple substorms on the buildup of the ring current, *J. Geophys. Res.*, *110*, A08202, doi:10.1029/2004JA010747.

Khalipov, V. L., Y. I. Galperin, A. E. Stepanov, and L. V. Shestakova (2001), Formation of a polarization jet during the expansion phase of a substorm: Results of ground-based measurements, *Cosmic Res., Engl. Transl.*, *39*, 226–235.

Kuznetsova, M. M., M. Hesse, L. Rastätter, A. Taktakishvili, G. Toth, D. L. De Zeeuw, A. Ridley, and T. I. Gombosi (2007), Multiscale modeling of magnetospheric reconnection, *J. Geophys. Res.*, *112*, A10210, doi:10.1029/2007JA012316.

Laitinen, T. V., M. Palmroth, T. I. Pulkkinen, P. Janhunen, and H. E. J. Koskinen (2007), Continuous reconnection line and pressure-dependent energy conversion on the magnetopause in a global MHD model, *J. Geophys. Res.*, *112*, A11201, doi:10.1029/2007JA012352.

Lemon, C., R. A. Wolf, T. W. Hill, S. Sazykin, R. W. Spiro, F. R. Toffoletto, J. Birn, and M. Hesse (2004), Magnetic storm ring current injection modeled with the Rice Convection Model and a self-consistent magnetic field, *Geophys. Res. Lett.*, *31*, L21801, doi:10.1029/2004GL020914.

Liemohn, M. W., J. U. Kozyra, V. K. Jordanova, G. V. Khazanov, M. F. Thomsen, and T. E. Cayton (1999), Analysis of early phase ring current recovery mechanisms during geomagnetic storms, *Geophys. Res. Lett.*, *26*, 2845–2848, doi:10.1029/1999GL900611.

Liu, W. W. (2006), Heat flux in magnetospheric convection: A calculation based on adiabatic drift theory, *Geophys. Res. Lett.*, *33*, L19104, doi:10.1029/2006GL027218.

Lui, A. T. Y. (2003), Inner magnetospheric plasma pressure distribution and its local time asymmetry, *Geophys. Res. Lett.*, *30*(16), 1846, doi:10.1029/2003GL017596.

Lyon, J. G., J. A. Fedder, and C. M. Mobarry (2004), The Lyon-Fedder-Mobarry (LFM) global MHD magnetospheric simulation code, *J. Atmos. Sol. Terr. Phys.*, *66*, 1333–1350, doi:10.1016/j.jastp.2004.03.020.

Mishin, E. V., and V. M. Mishin (2007), Prompt response of SAPS to stormtime substorms, *J. Atmos. Sol. Terr. Phys.*, *69*, 1233–1240, doi:10.1016/j.jastp.2006.09.009.

Moore, T. E., M.-C. Fok, D. C. Delcourt, S. P. Slinker, and J. A. Fedder (2008), Plasma plume circulation and impact in an MHD substorm, *J. Geophys. Res.*, *113*, A06219, doi:10.1029/2008JA013050.

Ober, D. M., N. C. Maynard, and W. J. Burke (2003), Testing the Hill model of transpolar potential saturation, *J. Geophys. Res.*, *108*(A12), 1467, doi:10.1029/2003JA010154.

Peymirat, C., and D. Fontaine (1994), Numerical simulation of magnetospheric convection including the effect of field-aligned currents and electron precipitation, *J. Geophys. Res.*, *99*, 11,155–11,176, doi:10.1029/93JA02546.

Powell, K. G., P. L. Roe, T. J. Linde, T. I. Gombosi, and D. L. de Zeeuw (1999), A solution-adaptive upwind scheme for ideal magnetohydrodynamics, *J. Comput. Phys.*, *154*, 284–309, doi:10.1006/jcph.1999.6299.

Pulkkinen, T. I., D. N. Baker, M. Wiltberger, C. Goodrich, R. E. Lopez, and J. G. Lyon (1998), Pseudobreakup and substorm onset: Observations and MHD simulations compared, *J. Geophys. Res.*, *103*, 14,847–14,854, doi:10.1029/97JA03244.

Raeder, J., D. Larson, W. Li, E. L. Kepko, and T. Fuller-Rowell (2008), OpenGGCM Simulations for the THEMIS Mission, *Space Sci. Rev.*, *141*, 535–555, doi:10.1007/s11214-008-9421-5.

Rasmussen, C. E., and R. W. Schunk (1987), Ionospheric convection driven by NBZ currents, *J. Geophys. Res.*, *92*, 4491–4504, doi:10.1029/JA092iA05p04491.

Rastätter, L., M. Hesse, M. Kuznetsova, J. B. Sigwarth, J. Raeder, and T. I. Gombosi (2005), Polar cap size during 14-16 July 2000 (Bastille Day) solar coronal mass ejection event: MHD modeling and satellite imager observations, *J. Geophys. Res.*, *110*, A07212, doi:10.1029/2004JA010672.

Ridley, A., T. Gombosi, and D. Dezeeuw (2004), Ionospheric control of the magnetosphere: Conductance, *Ann. Geophys.*, *22*, 567–584.

Ridley, A. J., and E. A. Kihn (2004), Polar cap index comparisons with AMIE cross polar cap potential, electric field, and polar cap area, *Geophys. Res. Lett.*, *31*, L07801, doi:10.1029/2003GL019113.

Ridley, A. J., and M. W. Liemohn (2002), A model-derived storm time asymmetric ring current driven electric field description, *J. Geophys. Res.*, *107*(A8), 1151, doi:10.1029/2001JA000051.

Ridley, A. J., D. L. De Zeeuw, T. I. Gombosi, and K. G. Powell (2001), Using steady state MHD results to predict the global state of the magnetosphere-ionosphere system, *J. Geophys. Res.*, *106*, 30,067–30,076, doi:10.1029/2000JA002233.

Roelof, E. C. (1987), Energetic neutral atom image of a storm-time ring current, *Geophys. Res. Lett.*, *14*, 652–655, doi:10.1029/GL014i006p00652.

Rusanov, V. V. (1970), On difference schemes of third order accuracy for nonlinear hyperbolic systems, *J. Comput. Phys.*, *5*, 507–516.

Sckopke, N. (1966), A general relation between the energy of trapped particles and the disturbance field near the Earth, *J. Geophys. Res.*, *71*, 3125–3130.

Sheldon, R. B., and D. C. Hamilton (1993), Ion transport and loss in the earth's quiet ring current. I - Data and standard model, *J. Geophys. Res.*, *98*, 13,491, doi:10.1029/92JA02869.

Siscoe, G. L., R. L. McPherron, and V. K. Jordanova (2005), Diminished contribution of ram pressure to Dst during magnetic storms, *J. Geophys. Res.*, *110*, A12227, doi:10.1029/2005JA011120.

Song, P., D. L. DeZeeuw, T. I. Gombosi, C. P. T. Groth, and K. G. Powell (1999), A numerical study of solar wind-magnetosphere interaction for northward interplanetary magnetic field, *J. Geophys. Res.*, *104*, 28,361, doi:10.1029/1999JA900378.

Song, Y., S. Sazykin, and R. A. Wolf (2008), On the relationship between kinetic and fluid formalisms for convection in the inner magnetosphere, *J. Geophys. Res.*, *113*, A08216, doi:10.1029/2007JA012971.

Southwood, D. J. (1977), The role of hot plasma in magnetospheric convection, *J. Geophys. Res.*, *82*, 5512–5520, doi:10.1029/JA082i035p05512.

Southwood, D. J., and R. A. Wolf (1978), An assessment of the role of precipitation in magnetospheric convection, *J. Geophys. Res.*, *83*, 5227–5232, doi:10.1029/JA083iA11p05227.

Spiro, R. W., R. A. Heelis, and W. B. Hanson (1978), Ion convection and the formation of the mid-latitude F region ionization trough, *J. Geophys. Res.*, *83*, 4255–4264, doi:10.1029/JA083iA09p04255.

Taktakishvili, A., M. M. Kuznetsova, M. Hesse, M.-C. Fok, L. Rastätter, M. Maddox, A. Chulaki, T. I. Gombosi, and D. L. De Zeeuw (2007a), Buildup of the ring current during periodic loading-unloading cycles in the magnetotail driven by steady southward interplanetary magnetic field, *J. Geophys. Res.*, *112*, A09203, doi:10.1029/2007JA012317.

Taktakishvili, A., M. Kuznetsova, M. Hesse, L. Rastätter, A. Chulaki, and A. Pulkkinen (2007b), Metrics analysis of the coupled Block Adaptive-Tree Solar Wind Roe-Type Upwind Scheme and Fok ring current model performance, *Space Weather*, *5*, S11004, doi:10.1029/2007SW000321.

Taktakishvili, A., M. M. Kuznetsova, M. Hesse, M.-C. Fok, L. Rastätter, M. Maddox, A. Chulaki, G. Tóth, T. I. Gombosi, and D. L. De Zeeuw (2008), Role of periodic loading-unloading in the magnetotail versus interplanetary magnetic field B_z flipping in the ring current buildup, *J. Geophys. Res.*, *113*, A03206, doi:10.1029/2007JA012845.

Toffoletto, F., S. Sazykin, R. Spiro, and R. Wolf (2003), Inner magnetospheric modeling with the Rice Convection Model, *Space Sci. Rev.*, *107*, 175–196, doi:10.1023/A:1025532008047.

Toffoletto, F. R., S. Sazykin, R. W. Spiro, R. A. Wolf, and J. G. Lyon (2004), RCM meets LFM: Initial results of one-way coupling, *J. Atmos. Sol. Terr. Phys.*, *66*, 1361–1370, doi:10.1016/j.jastp.2004.03.022.

Tóth, G., et al. (2005), Space weather modeling framework: A new tool for the space science community, *J. Geophys. Res.*, *110*, A12226, doi:10.1029/2005JA011126.

Tsyganenko, N. A., and T. Mukai (2003), Tail plasma sheet models derived from Geotail particle data, *J. Geophys. Res.*, *108*(A3), 1136, doi:10.1029/2002JA009707.

van Leer, B. (1979), Towards the ultimate conservative difference scheme. V. A second-order sequel to Godunov's Method, *J. Comput. Phys.*, *32*, 101–136.

Vasyliunas, V. M. (1970), Mathematical models of magnetospheric convection and its coupling to the ionosphere, in *Particles and Field in the Magnetosphere*, *Astrophys. Space Sci. Libr.*, vol. 17, p. 60, Springer, New York.

Vasyliunas, V. M. (2006), Ionospheric and boundary contributions to the Dessler-Parker-Sckopke formula for Dst, *Ann. Geophys.*, *24*, 1085–1097.

Wanliss, J. A., and K. M. Showalter (2006), High-resolution global storm index: Dst versus SYM-H, *J. Geophys. Res.*, *111*, A02202, doi:10.1029/2005JA011034.

Weimer, D. R. (2001), An improved model of ionospheric electric potentials including substorm perturbations and application to the Geospace Environment Modeling November 24, 1996, event, *J. Geophys. Res.*, *106*, 407–416, doi:10.1029/2000JA000604.

Welling, D. (2009), Exploring sources of magnetospheric plasma using the validated SWMF, Ph.D. thesis, Univ. of Mich., Ann Arbor.

Wolf, R. A., R. W. Spiro, S. Sazykin, and F. R. Toffoletto (2007), How the Earth's inner magnetosphere works: An evolving picture, *J. Atmos. Sol. Terr. Phys.*, *69*, 288–302, doi:10.1016/j.jastp.2006.07.026.

Yang, J., F. R. Toffoletto, R. A. Wolf, S. Sazykin, R. W. Spiro, P. C. Brandt, M. G. Henderson, and H. U. Frey (2008), Rice Convection Model simulation of the 18 April 2002 sawtooth event and evidence for interchange instability, *J. Geophys. Res.*, *113*, A11214, doi:10.1029/2008JA013635.

Zaharia, S., V. K. Jordanova, M. F. Thomsen, and G. D. Reeves (2006), Self-consistent modeling of magnetic fields and plasmas in the inner magnetosphere: Application to a geomagnetic storm, *J. Geophys. Res.*, *111*, A11S14, doi:10.1029/2006JA011619.

Zhang, J., et al. (2007), Understanding storm-time ring current development through data-model comparisons of a moderate storm, *J. Geophys. Res.*, *112*, A04208, doi:10.1029/2006JA011846.

Zhang, J. C., R. A. Wolf, R. W. Spiro, G. M. Erickson, S. Sazykin, F. R. Toffoletto, and J. Yang (2009), Rice Convection Model simulation of the substorm-associated injection of an observed plasma bubble into the inner magnetosphere: 2. Simulation results, *J. Geophys. Res.*, *114*, A08219, doi:10.1029/2009JA014131.

Zheng, Y., A. T. Y. Lui, and M. Fok (2008), Viewing perspective in energetic neutral atom intensity, *J. Geophys. Res.*, *113*, A09217, doi:10.1029/2008JA013070.

Zou, S., L. R. Lyons, C.-P. Wang, A. Boudouridis, J. M. Ruohoniemi, P. C. Anderson, P. L. Dyson, and J. C. Devlin (2009), On the coupling between the Harang reversal evolution and substorm dynamics: A synthesis of SuperDARN, DMSP, and IMAGE observations, *J. Geophys. Res.*, *114*, A01205, doi:10.1029/2008JA013449.

P. C. Brandt, Johns Hopkins University Applied Physics Laboratory, 11100 Johns Hopkins Rd., Laurel, MD 20723-6099, USA.

N. Buzulukova, M.-C. Fok, A. Glocer, M. Kuznetsova, T. E. Moore, A. Pulkkinen, and L. Rastätter, NASA Goddard Space Flight Center, Mail Code 673, Bldg. 21/261b, 8800 Greenbelt Rd., Greenbelt, MD 20771, USA. (nbuzulukova@gmail.com)

G. Tóth, Center for Space Environment Modeling, University of Michigan, Ann Arbor, MI 48109-2143, USA.